Spring 2022

A Study of Reduced Activation Ferritic Martensitic Metal Core Wire for Wire Arc Additive Manufacturing

Alexander L. Reichenbach

Recommended Citation

Reichenbach, Alexander L., "A Study of Reduced Activation Ferritic Martensitic Metal Core Wire for Wire Arc Additive Manufacturing" (2022). *Electronic Theses and Dissertations*. 2437.
https://digitalcommons.georgiasouthern.edu/etd/2437

A STUDY OF REDUCED ACTIVATION FERRITIC MARTENSITIC METAL CORE WIRE FOR WIRE ARC ADDITIVE MANUFACTURING

by

ALEX REICHENBACH

(Under the Direction of Bishal Silwal)

ABSTRACT

This study seeks to determine the technical feasibility of fabricating reduced activation ferritic martensitic (RAFM) steel parts using a wire arc additive manufacturing (WAAM) process. The WAAM process manufactures a part by depositing layers of metal onto a substrate to build a large scale near net shape part. RAFM alloy steels are next-generation steels designed to resist radiation effects in the radiation intense working environments, such as nuclear reactors. To achieve this, process development and testing to create the WAAM production process with the custom RAFM filler wire were carried out. Several welding waveform modes were tested, and it was determined that Pulse waveform mode offers an acceptable weld parameter to fabricate custom made RAFM metal cored wire successfully. The first test walls were hardness tested, and metallography was conducted to categorize the microstructure present in the steel. Continued analysis was performed on samples with controlled interpass temperatures. The microstructure present is typical martensitic lath, and the presence of delta ferrite is inevitable. The settings were further tested with the addition of shielding gas experimentation to determine if the porosity visible in the initial prints could be removed. The shielding gas results did aid in the porosity control but introduced other issues that arose. With a reduction in amperage input from the initial settings and the addition of wait times allowing the equipment to cool, large scale prints were successfully fabricated. The mechanical properties of the deposited material were tested, such as impact toughness, macro, and microhardness. These tests resulted in an average impact absorption energy of 6.25J and an average hardness across two-layer deposition interpass test samples of 423.74HV.

INDEX WORDS: Thesis, Additive manufacturing, Arc welding, Robotics, WAAM, RAFM, Georgia Southern University.

A STUDY OF REDUCED ACTIVATION FERRITIC MARTENSITIC METAL CORE WIRE FOR WIRE ARC ADDITIVE MANUFACTURING

by

ALEX REICHENBACH

B.S., Georgia Southern University, 2020

M.S., Georgia Southern University, 2022

A Thesis Submitted to the Graduate Faculty of Georgia Southern University

in Partial Fulfillment of the Requirements for the Degree

MASTER OF SCIENCE

ALLEN E. PAULSON COLLEGE OF ENGINEERING AND COMPUTING

A STUDY OF REDUCED ACTIVATION FERRITIC MARTENSITIC METAL CORE WIRE FOR WIRE ARC ADDITIVE MANUFACTURING

by

ALEX REICHENBACH

Major Professor:	Bishal Silwal
Committee:	Mingzhi Xu
	Haijun Gong
	JingJing Qing

Electronic Version Approved:

May 2022

DEDICATION

This paper is dedicated to my Mother and Father who have supported and provided for me in my academic journey.

ACKNOWLEDGMENTS

I would like to acknowledge motivation and informative guidance Dr. Shaowen Xu, and Dr. Brian Vlcek bestowed upon me. The practical assistance given to me by, Mr. Chris Gerdman, Mr. Andrew Michaud, and Mr. Jeff Hoopes. And the undergraduate lab mates who worked with me conducting this research: Marcus Perez, Sam Hagler, and Daniel Johnson.

TABLE OF CONTENTS

LIST OF TABLES

LIST OF FIGURES

CHAPTER 1: INTRODUCTION

1.1 Background

WAAM, wire arc additive manufacturing, is a metal additive manufacturing solution rapidly gaining popularity due to its low cost, rapid production time, and ability to be scaled easily. The use of such technology is far-reaching, and when combed with other specific types of production, such as high-cost materials, the overall production costs can be lowered. For example, a custom alloy metal is used for the feedstock, decreasing the raw material cost. The GMAW, Gas Metal Arc Welding, also known as metal inert gas welding, is a ubiquitous welding process and the one selected for this WAAM study. The production process is designed to 3D print parts near-final geometry, which reduces material waste. The RAFM, reduced activation ferritic martensitic steel, is being developed as a next-generation material for nuclear fusion reactor applications. Irradiation effects on metals, such as a loss in fracture toughness, void swelling, embrittlement, irradiation creep, and stress relaxation, are all adverse effects. They can be accounted for; decreasing or eliminating them is desired (Chopra, O.K. & Rao, A.S. 2011). RAFM alloys are strong martensite formers, the hardest and subsequently most brittle phase of steel alloys. RAFM alloys are designed to resist these adverse effects, as well as the ability to maintain their strength in high heat working conditions, commonly associated with these radiation intense environments. Further emphasis on removing active elements from the material composition is to decrease the residual radiation in the metals to lower the waste level and decrease recycling time. The low barriers to entry of WAAM and added cost-saving benefits of the process are helping to provide for more access to new generation metallurgical technologies when in use with other specialized materials.

1.2 Motivation:

The study assesses the possibility of combining a manufacturing process and next-generation high alloy steels to produce a net shape part. The alloy steel is a custom specification based on the early development of next-generation steels for nuclear fusion reactor applications. Still, it has not been used in this way due to the cost and commercial availability. Most RAFM-related studies have been carried out using samples from a small number of cast production runs. The combination of RAFM steels and fusion welding has had minimal research done, and WAAM production capabilities have not been studied.

1.3 Objectives:

The main goal of this research is to study the technical feasibility of fabricating RAFM steel parts using the WAAM process. To achieve the goal, the Thesis has the following objectives (1) Develop a WAAM process used to produce RAFM steel sample parts. (1.1) Test the power source waveform control technology to dissect further and improve the deposition process. (2) Examine the effects of heat cycling and interpass temperature on grain formation and reformation. Specifically, the martensite formation, to determine the grain structure and tempering effects that can be observed after the deposition process. (4) Test various mechanical properties of the produced material samples.

CHAPTER 2: LITERATURE REVIEW

2.1 Overview

The literature review contains the background information relevant to the wire-arc Additive Manufacturing process employed, the high alloy steel used, and its applications, along with arc welding processes that have been developed for this application and testing criteria to examine the material's mechanical properties.

2.2 WAAM

WAAM or Wire Arc Additive Manufacturing is a subcategory of Directed Energy Deposition, which can generally be grouped under the umbrella of 3D printing. WAAM typically uses a welding power source to produce an electric arc intended to melt a feed wire stock, making relatively cost-effective near-final geometry metallic parts. Compared to other additive manufacturing processes, WAAM can achieve a moderately high deposition rate, unlike powdered bed fusion. The size and complexity of part production can vary greatly and are primarily based on equipment capabilities but are generally considered mid to large scale and low to medium geometric complexity. The low cost of welding wire relative to metal powders is a further cost-saving benefit for operation costs and startup cost savings. These lower barriers to entry and other non-tangible benefits of AM and DED have made it more accessible to manufacturers and significantly increased use and active research with the technology. (ASTM, 2015)

WAAM relies on an automated welding process such as gas metal arc welding, GMAW/MIG, or gas tungsten arc welding, GTAW/TIG. These are the two most used welding processes because of their low cost, off-the-shelf, equipment options available that a WAAM system can efficiently be designed with, as opposed to other arc welding processes (Williams, et al. 2016). MCAW, or Metal Core Arc Welding, is a variation of MIG arc welding whereby the standard solid metal wire is replaced with a powdered metal core wire; however, the fundamentals of the process otherwise remain the same. MIG is a consumable electrode process allowing the apparatus to be more compact when compared to TIG, which has a separate electrode and deposition material source. This simplicity is beneficial outside of cost because the more compact welding torch can simplify robot programming and aid in complex geometry production.

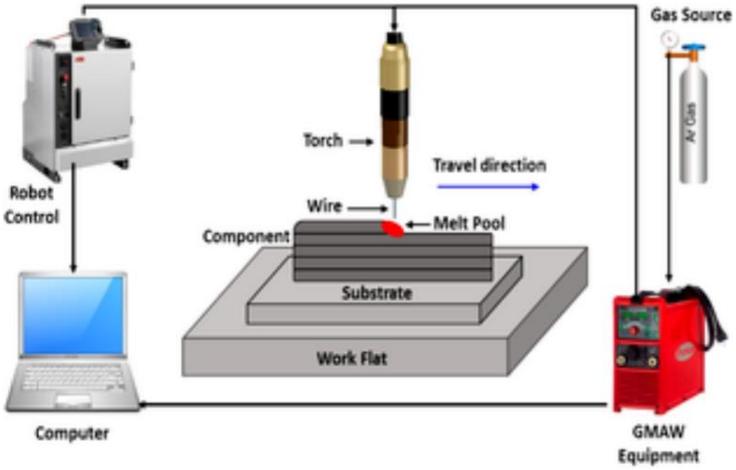

Figure 1: Basic WAAM component diagram (Xia, et al. 2020)

The fusion-based arc welding process, as it applies to WAAM, is performed in a way that weld beads are stacked successively on top of each other to build a near-net part. A near net part will require finish machining to satisfy some, or all, of the original dimensional specifications (Tiago A. Rodrigues 2019). Although this machining is subtractive, the amount necessitated to complete the part is far less than a fully machined subtractive manufacturing process would require. While a large amount of information about arc welding is known, its application to additive manufacturing presents further challenges to consider. Tool path optimizing is a crucial step to the success of a print. Some studies have shown the effectiveness of actively cooling the part during the manufacturing process. This can help minimize residual stress and control of microstructure, which is being reformed by the continuous directional heat applied throughout multiple deposition layers (Leandro, et al. 2020).

2.3 RAFM Steels

Reduced Activation Ferritic Martensitic (RAFM) steels are a type of high alloy steel designed to be used in radiation intense environments, such as a nuclear fusion reactor. RAFM steels have different names depending on where it is being developed; however, the differences extend further than the surface. In the EU, higher chromium and lower tungsten composition are referred to as Eurofer (or Eurofer97), selected to improve corrosion resistance and decrease neutron adsorption. Designations found in other countries: Chinese CLAM: Chinese Low Activation Martensitic steel, Indian INRAM: Indian Reduced Activation Ferritic Martensitic steel, Korea ARAA: Advanced Reduced Activation Alloy, are all similar in alloying composition. As well as Russia, RUSFER: Russian Reduced Activation Material is known to be under development. The United States has been developing RAFM steels with higher strength and improved radiation resistance with applicable temperatures up to 600–650C, much of this development taking place at Oakridge National Lab (Tavassoli, et al. 2014)

In early Eurofer testing and experimentation, the impurity control level was not as precise as desired but can still be considered Low-Level Waste 100 years after service. With better impurity control measures, such as dedicated production lines, the material can theoretically be improved to Hands-on Level Domain, which requires simple burial and not underground encapsulation for recycling (Seidle, et al. 2002).

Table 1: Alloying Elements in various RAFM compositions, undesirable elements measured in ppm, major elements measured in weight percent (Tavassoli, et al. 2014)

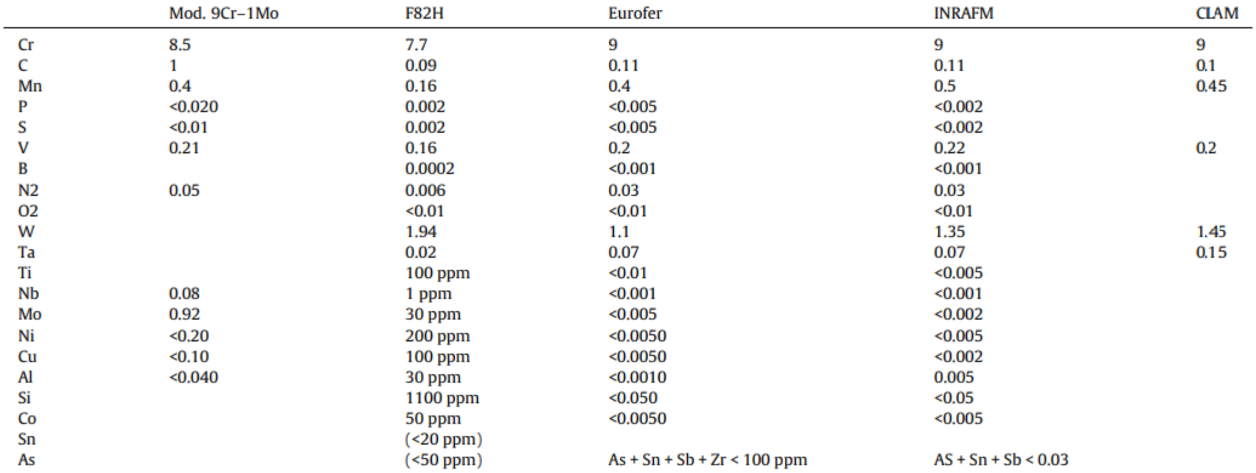

	Mod. 9Cr–1Mo	F82H	Eurofer	INRAFM	CLAM
Cr	8.5	7.7	9	9	9
C	1	0.09	0.11	0.11	0.1
Mn	0.4	0.16	0.4	0.5	0.45
P	<0.020	0.002	<0.005	<0.002	
S	<0.01	0.002	<0.005	<0.002	
V	0.21	0.16	0.2	0.22	0.2
B		0.0002	<0.001	<0.001	
N2	0.05	0.006	0.03	0.03	
O2		<0.01	<0.01	<0.01	
W		1.94	1.1	1.35	1.45
Ta		0.02	0.07	0.07	0.15
Ti		100 ppm	<0.01	<0.005	
Nb	0.08	1 ppm	<0.001	<0.001	
Mo	0.92	30 ppm	<0.005	<0.002	
Ni	<0.20	200 ppm	<0.0050	<0.005	
Cu	<0.10	100 ppm	<0.0050	<0.002	
Al	<0.040	30 ppm	<0.0010	0.005	
Si		1100 ppm	<0.050	<0.05	
Co		50 ppm	<0.0050	<0.005	
Sn		(<20 ppm)			
As		(<50 ppm)	As + Sn + Sb + Zr < 100 ppm	AS + Sn + Sb < 0.03	

RAFM steels are necessary to improve nuclear reactors; many otherwise unique issues present themselves when materials are exposed to such radiation intense environments. One of those is irradiation embrittlement, where a material DBTT, Ductile to Brittle Transition Temperature, is lowered because of the radiation exposure. Another is irradiation swelling, where the material increases in size, sometimes to the point of necessary consideration in part design and production to prevent damage. In previous generation steels such as austenitic stainless, such as Type 316L, high doses of radiation-induced swelling as much as 5% were experienced, along with other adverse mechanical property effects (Tavassoli, et al. 1993).

Early on, the study of reduced activation steels became significant when it was determined that 'no-activation' steels would be impossible. Through testing and nuclear calculations, the elimination or replacement of Mo, Nb, Ni, Cu, and N would be advantageous.

These elements were substituted with Tungsten and Vanadium for Molybdenum and Tantalum for Niobium (Klueh and Bloom 1985). Different Chromoly compositions were also considered, but disadvantages were found with higher Cr content. With Cr 12%, eliminating δ-ferrite became difficult without a subsequent increase in carbon or manganese for austenite stabilization. The δ-ferrite may be ideal because of its lower toughness and the manganese increasing radiation embrittlement (Gelles, et al. 1990). The lower Cr steels, around 2.25% Cr, had increased carbide precipitation making them more prone to irradiation hardening at elevated temperatures, significantly weakening them (Hamilton and Gelles 1987) (Basuki and Aktaa 2010).

The largest precipitates in 9Cr ODS are M23C6-type carbides, precipitating along the austenitic grains; they consist of Fe, C, Cr, Mo, and V; these carbides are very important in the heat-resistant steels for the initial microstructural stability by pinning the movement of grain boundaries and inhibiting the recrystallization. However, it is frequently revealed that M23C6 carbides exhibit a high coarsening rate during long-term creep and aging at high temperatures (Zheng et al. 2020). In CLAM samples, ellipsoid-shape and spherical-shape MX carbonitrides are seen in untreated states. This fine spherical-shape MX carbonitrides could be the mechanism improving the mechanical properties of CLAM steel, especially creep strength (Wang, Xu, and Song 2019). It was further tested that during aging, at an elevated temperature of 550 °C, the phases continued to precipitate larger, and a new Laves phase was introduced after a considerable aging time when examining the long-term effects of high temperatures found in fusion reactors.

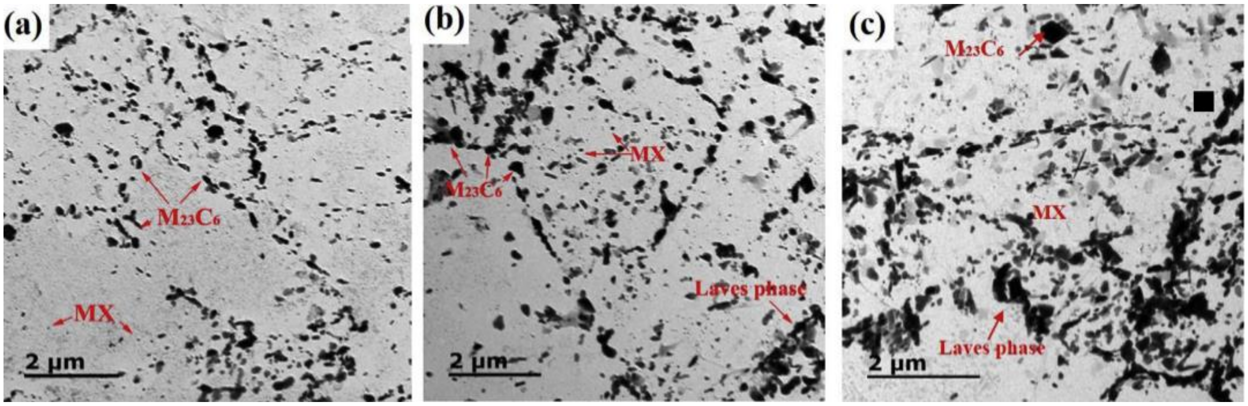

Figure 2: CLAM Precipitates in optical microscope, (a) 0h, (b) 10,000h, (c) 20,000h (W. Wang, Xu, and Song 2019)

2.4 Wire Selection

There are three types of welding wires: solid, flux-cored, and metal-cored; because RAFM alloy steels are not commercially available, having welding wire made with it presented a unique challenge. Without a sizeable initial investment, a custom alloy solid wire is not possible to have produced as it would require a substantial quantity. Additional challenges would also need to be overcome in solid wire production, such as the potential contamination introduced during the casting and hot rolling production process before the wire-specific production steps have begun. The main interest factor behind powdered metal-cored wire is cost. Standard vs. powdered metal core wire is still relatively expensive; when comparing the cost of solid ER70S weld wire to a metal-cored ER70C version, the price is two times more costly to purchase, $4 per pound vs. 8$ per pound respectively. At the same time, both options are still readily available. Even with the unit cost being higher, the ability to purchase small-sized production batches, in the order of a few thousand dollars, means the overall cost is greatly reduced. Compared to spending hundreds of thousands of dollars for a full production run of a custom alloy to be rolled into solid wire, this scenario is more cost beneficial for many instances, such as this research study.

Cored welding wire is produced with a rolling and drawing process; while some details are kept secret, the generic process has been used for a long time, originally designed to make flux core welding wire. Metal strips with about 15mm in width and thickness of about 1mm, size varying depending on the desired final wire diameter, are the first material needed in the wire production process, which themselves were produced via some combination of continuous casting and hot or cold rolling prior, as seen in Figure 2. The first step begins by forming the metal strip into a "U" shape, proceeded by the desired powders being deposited into the U slot. After which the closing procedure takes place, this may vary based on the manufacturer and the desired seam type; the two primary methods of closing the wire are seamed and seamless. Seamed is a folded or mated edge of both open sides, typically with an overlap. Seamless is generally performed with an in-line laser to weld the sides together. Once this is complete additional rolling and drawing processes are used to achieve the final desired wire diameter, and some form of heat treatment to relieve any coldworking stress and surface treatment to preserve the wire may be applied.

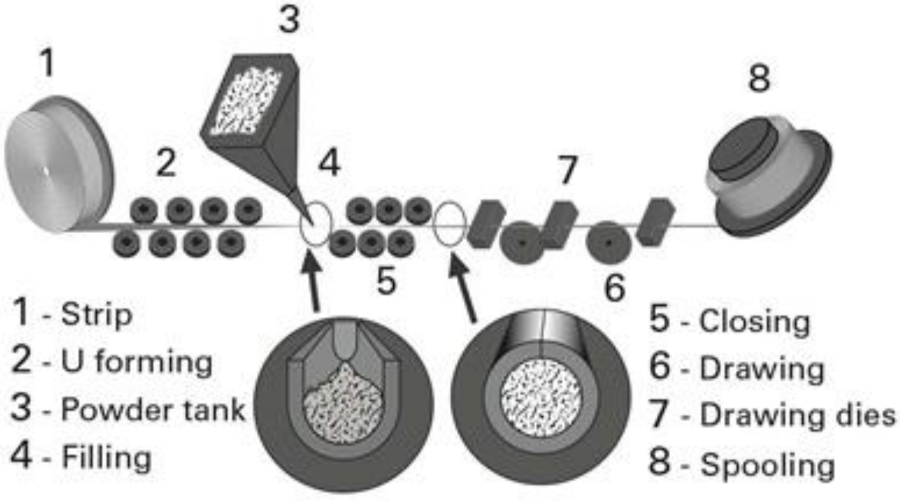

Figure 3: Metal core wire production method, adapted from (Bellini, Vezzue, Scappin. 2018)

There are some secondary benefits as to why metal core wire may be selected in other instances when not required. The ease of customizability allows researchers to test and tailor specific chemistries to their needs, enabling minor and iterative improvements to be made through the development process. Additionally, the deposition rate and efficiency of powdered metal core wires are increased to that of solid core wires in certain conditions. It was found when comparing ER70 based .045” dia. wires: solid (ER70S6), basic flux-cored (E70T5CJH4), rutile flux-cored (E71T1MH4), metal-cored (E70C6MH4), and low fume metal-cored (E70C6MH4). The highest deposition efficiency rates were achieved with the metal-cored wire, also suggesting that the low fume variant would further benefit the welder’s safety (Gheonea, et al. 2018).

2.5 Arc Welding Selection

The WAAM process does not always require highly specific weld parameters, but the wire alloy used and geometric properties desired are the leading factors in process execution choices. The simplicity of the selected welding process is a significant advantage to WAAM; one of the more common choices for the arc welding process is MIG welding. It provides a great range of capabilities with modern inverter-based machines, including different variations of MIG welding like metal-core arc welding or MCAW. They also offer more simple control methods for welding, such as synergistic modes where most of the parameters are auto calculated for the user based on a select few inputs. Different power delivery modes allow even finer adjustments to the arc welding process, such as frequency tuning.

There are three primary metal transfer modes in MIG/MCAW arc welding: Dip transfer (short circuit), Globular transfer, and Spray transfer (axial spray). Dip transfer is when the wire feeds faster than it can arc, so the wire dips into the weld pool, creating a short circuit to form the arc. Dip transfer is a relatively low energy process and can be defined by its small weld pool and lack of penetration depth, which is commonly used in manual MIG welding. The globular transfer is a middle power transfer mode where large balls, or globs, of molten metal are formed at the tip of the wire. A short circuit is not experienced during the transfer, as gravity overcoming the surface tension of the glob creates the transfer mechanism. This method creates an excess of spatter due to the turbulence and subsequent causes a decrease in the deposition rate of the metal, which is a major drawback of this transfer mode. Spray transfer is when the wire melts quickly into the arc and is carried to the weld pool by gravity and the arc at a very high rate; this high-energy, high heat process is characterized by its deep penetration and high deposition rate.

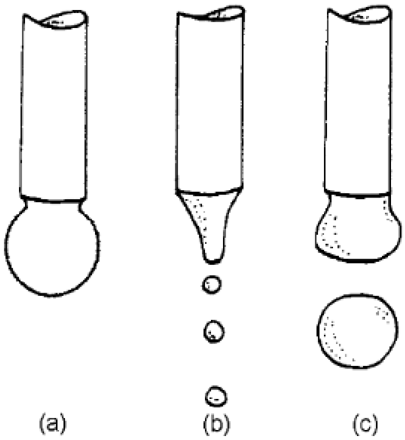

Figure 4: GMAW transfer modes: (a) globular, (b) spray, and (c) pulse (Praveen, Yarlagadda, Kang. 2005)

Further variations of these standard welding modes have also been developed, such as STT, surface tension transfer, or pulsed spray transfer. STT is a pulsed current waveform that uses the low current and surface tension to force the droplets to the weld pool; this is a lower heat process and is preferable for welding thinner materials. (Akers, R. Anderson, P. Barrett, M. 2015) Pulse spray combines dip and sprays transfer modes by pulsing amperage and voltage to switch back and forth between the two at high frequency; this enables better penetration than dip transfer and lower overall energy/heat input than spray transfer alone. And the further potential benefit of allowing welding out of standard torch positions more easily. This study observed that Power Mode's longer, flatter region after peak, signifying droplet release, improves current control over CV. The drops current during a short in STT lowers the heat input into the weld compared to CV. Lower heat input, as observed in STT is desired for WAAM applications because the task of rapidly depositing weld beads on top of one another causes massive heat buildup; alleviating this in any way possible is beneficial (Akers, Anderson, Barrett. 2015).

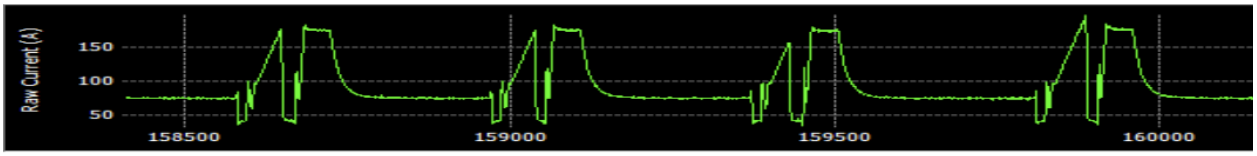

STT ® waveform

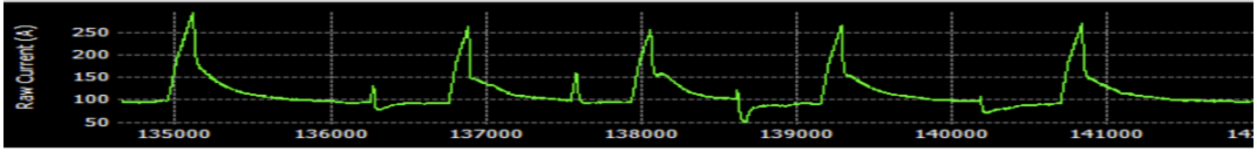

Power Mode ™ Waveform

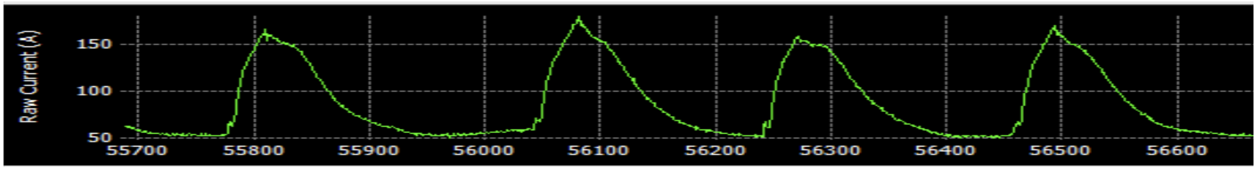

CV Waveform

Figure 5: Lincoln PowerwaveTM observer data, comparing STT, Power Mode, and Constant Voltage Waveform (Akers, Anderson, Barrett. 2015)

Modern inverter-based welding power sources offer other benefits to weld process development; they commonly allow the user to examine the waveform of the welding process to tune further and diagnose the output. With the real-time data provided, a more insightful approach can be taken to the weld’s performance, and active monitoring of the welding process can translate to improved product quality.

Pulse current can provide additional benefits to WAAM processes. Including reduced heat input, reduced spatter and fume generation, and energy savings. The lower heat input of current oscillation allows for a decrease in the size of the HAZ in traditional welding scenarios; this may provide benefits in reducing the warpage and directional heating/cooling effect during the manufacturing process. The spatter reduction is derived from the observed ability of pulsed current to lower the amperage threshold of the metal spray transfer method; without the high pulsed current globular transfer would be occurring (Da, Vora, Patel, Bogum. 2021). The turbulence created in the weld pool of globular transfer also causes an increased amount of spatter, thereby decreasing the deposition efficiency, making it much less ideal for WAAM where the deposition rate is a critical factor in the efficiency of the process.

The creation of different transfer modes in GMAW is primarily driven by the current used in the process. This transition can be graphed to show the relationship between the molten droplet diameter and the current input. This transition is essential to note, as the function of pulse current mode is to exceed the globular transfer range and create a hybrid increased spray transfer droplet size while reducing the heat input overall by decreasing the current after the transfer of the droplet.

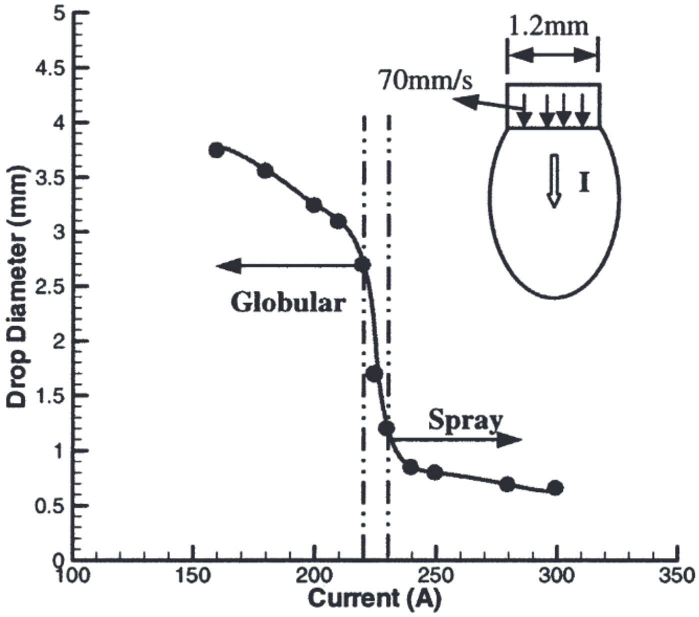

Figure 6: Current vs. Drop Diameter (Wang, Huang, Zhang. 2004)

2.6 Interpass temp

In standard arc welding, multipass welds are sometimes necessary. These multipass welds present unique challenges with controlling the microstructure of the weld and the substrate because of the repeated heat cycling. Each additional pass of the weld may cause discontinuities in the fusion zone and increase the size or decrease the strength of the heat affect zone. During the WAAM process, welds are continually being deposited on top of one another to build the designed part. This translates to a constant, often multidirectional, heat cycling process applied to already deposited material as the region is built up layer by layer. It will be important to know how the interpass temperature is related to the phase structure after the manufacturing process is completed.

With highly martensitic steels such as P92 Martensitic Heat Resistant Steel, controlling interpass temperature is very important to forming a uniform microstructure. According to Moravec, et al. (2016), to keep the fusion zone above the martensite start temperature, a preheat of 250ºC and an interpass temperature of 300ºC were selected. The experimental interpass temperature recorded was between 270-295ºC. This controlled temperature range resulted in a uniform hardness profile across the weld and up each layer of the multipass weld. In grade 91 steel, with a makeup of 9Cr-1Mo-V; studying HAZ’s after multipass weld and how toughness was altered a preheat of 150ºC and 250ºC and an interpass of 200ºC and 300ºC was used in conjunction with post weld heat treat (Silwal, et al. 2013). These temperatures were referenced for the studies experiemental procedures.

2.7 Metallography

Optical microscopes are one of the simplest and easiest ways to examine the crystalline structure of a material. Studying the material's morphology is an essential step to understanding the mechanical testing results. By identifying the phases present visually, a prediction of the mechanical properties can be formed; with RAFM, high levels of martensite should be observed, which indicates that a higher hardness will be measured. The size of the grains may also show the effect of heating and cooling cycles during the manufacturing process and the hardness measurements.

The comparison of welded and cast production RAFM steels is important to know. There will likely be major differences in the microstructure due to the localized cooling rates and processes. An 'as produced' vs. tempered RAFM sample, seen here in Figure 7, shows the dark regions, indicating martensite and white regions, residual ferrite. The residual ferrite in the tempered micrograph is unexpected because a fully martensitic structure would be expected in the normalizing treatment but can be seen as large white grains. Oxygen Dispersion Strengthened EUROFER: 8.92wt% Cr, 0.99wt% W, 0.15wt% Ta, 0.09wt% C.

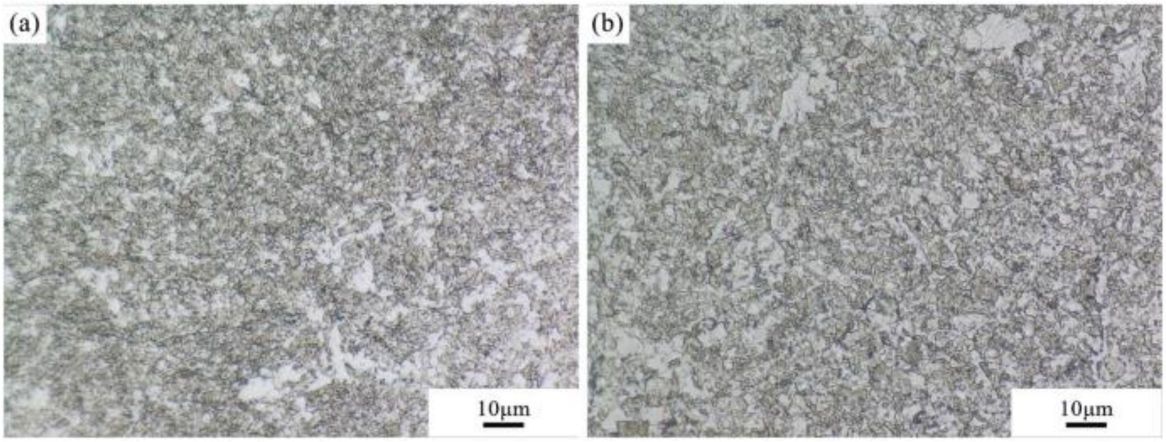

Figure 7: Optical Micrographs of (a) as produced and (b) tempered ODS EUROFER Steel (Fu, et al. 2020)

2.8 Mechanical Testing

General hardness testing, performed on the Rockwell scale, is not the most descriptive hardness testing available because it tests a relatively large area. To get more detailed information about the material's morphology, micro or nano hardness can be performed. Microhardness is beneficial because it can be mathematically correlated to the tensile strength of the material, and select grains can be tested to determine the hardness of specific phases, as well as help to differentiate between forms of the same phase like fresh vs. reformed martensite. As stated in Peng, et al. (2015), the microhardness of RAFM steels was measured as radiation dosage was increased to establish the trend where the irradiation temperature would have a more significant effect on the hardening than the radiation itself.

Based on Chen, et al. (2016), impact toughness was measured based primarily on the effect of increasing the Tantalum content in the RAFM steel composition. The addition of Ta was correlated to a sharp increase in the impact toughness, from 171 J to 323 J, when Ta was increased from 0 to 0.027wt%. This phenomenon was explained by the density of undissolved carbides increases leading to smaller prior austenite grain size. However, tensile strength was not found to differ with the change in Ta significantly. With only a small increase at the highest test temperature of 800ºC, which is attributed to an increased coarsening rate of M23C6 carbides, leading to a higher density of MX, improving the dislocation strengthening by pinning the dislocations and slowing the recovery process.

When comparing as-wrought Grade 91 steel, additively manufactured, and aged AM at 700ºC for 1 hour, the DBTT of the as deposited and aged AM samples are ~30% and 100% higher, respectively than the wrought Grade 91 sample. This increase indicates higher fracture toughness of the additively manufactured samples. When comparing the yield strength, it decreases after aging at 650ºC after 100hr, due to the annealing of the martensitic phases and general coarsening of the microstructure. However, yield strength does not decrease further, even when annealing up to 1000hr's (El-Atwani, et al. 2021).

Measuring impact toughness of CLF-1 steels, corresponding to the heat input during the welding process, the lowest impact energy recorded directly correlates to the formation of delta ferrite in the grain structure. Above 2.5% volume fraction of delta ferrite formation, which occurred at high heat input, failed with the lowest impact energy, as seen in Figure 8 (Wu et al. 2020). This study also examined how pre and post weld heat treatments would affect the hardness of the material. While welded metal hardness remained high throughout all tests, multi-cycle post-weld heat treat processes saw the most significant reduction in hardness. The Carbon atoms in the martensite gradually precipitated during the heat treatment causing the hardness reduction; when compared to the preheat-only test, the effect of preheating is minimal.

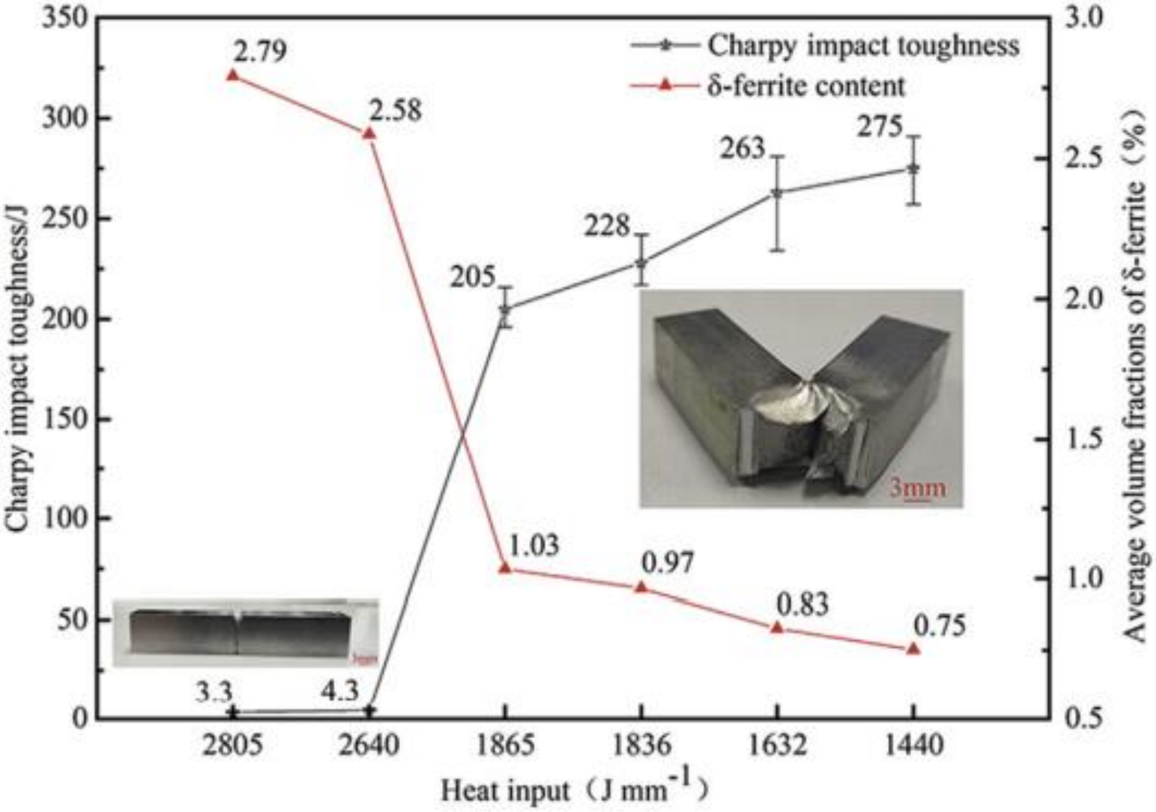

Figure 8: Heat input vs Charpy toughness and delta ferrite volume fraction (S. Wu et al. 2020a)

CHAPTER 3: RESEARCH METHODOLOGY

3.1 Methodology Overview

The methodology of this study is broken down into eight sections comprising equipment and software used to perform the manufacturing process, the WAAM process and how it applies to this study, the material science completed, and the mechanical testing conducted.

3.2 Equipment Employment and Usage

For the WAAM setup, a customized system was designed using off-the-shelf parts to function as the additive manufacturing machinery. This system is comprised of a robotic manipulator, welding power source, and automation kit to combine the power source and robot. The Robotic hardware consisted of a Kuka KR6 R900-Sixx robot arm with a KRC4 controller; this six-axis manipulator has a mechanical reach of about 1m from the mounting plate, which provides a large build area for producing parts. The arc welder used was a Lincoln Powerwave R450 with an autodrive wire feeder. The external wire feeder is attached to the table so cabling can run across the robot arm to the fixture. The standard .045" rollers in the wire feeder were removed in favor of ones designed explicitly for metalcore welding wire. The welder was adapted to the Kuka robot's mount plate using a Tregaskiss CA3 Tough Gun robotic MIG welding kit; this provided the welding wire cabling, gun/neck, and gun holding mount to the robot, as well as compatible welding consumables.

Figure 9: Welding cell used as experimental WAAM setup

The robot's programming was primarily done by hand, comprising simple loop statements and input coordinates as weld points. By creating data points in the workspace and adding weld statements between them, a single bead program can be built in minutes, which was very beneficial for the testing phase. This also allowed rapid programming and ease of code alteration to test a multitude of welding parameters. The offline programming software Octopuz was used for more intricate and precise paths. This software turned standard G code tool paths for 3D printing into KRL code for the robot. The programming control of the welder is incorporated into the controller and code with the use of Kuka's ArcTech Basic and ArcTech Advanced plugin packages. Welding code differs from standard movement code by replacing standard movement statements with arc prefixed commands. The weld type and data are assigned as variables across the program. The user must input the action points and robot movement type between the arc on and off commands to perform a weld. Multiple types of movement commands are available, allowing free range of movement.

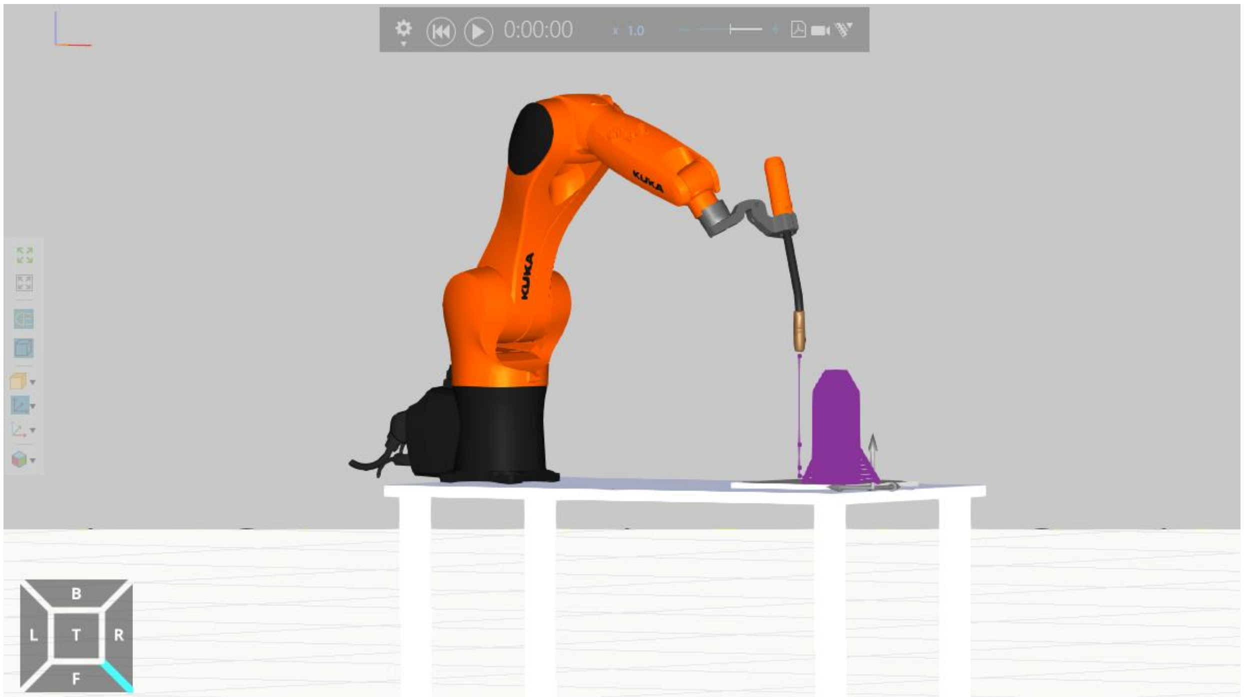

Figure 10: Virtual Welding cell in Octopuz to model code execution

3.3 Arc Welding Deposition

The Lincoln Electric power source has a wide range of methods and modes available; selecting wire type, size, and MIG or MCAW welding process eliminates many improper choices and provides a recommended baseline for the control parameters of the possible selections. Initial parameter testing was performed with single bead welds, which allowed a fast-cooling time and analysis of the weld. The primary weld modes were Power Mode®, Constant Voltage, and Pulse Mode®. Power Mode® is a given input wattage by the user, Constant voltage is a traditional MIG mode where the voltage is constant, and Pulse Mode® pulses the amperage and voltage based on a user input maximum amperage. Rapid Arc® was also tested as a variation of pulse mode with a more tuned waveform by Lincoln Electric. Since it was believed some form of pulse current would provide the best metal transfer, based on the literature review, multiple tests with different pulse variations were performed. These were also used to determine the effect trim and ultimate arc would have on the deposition. The test welds were categorized by the physical dimensions of the deposited material, uniformity, the level of spatter observed, heat buildup, and frequency of welder error during the process. These were also considered but not driving factors. After single bead welds were analyzed, two bead welds were deposited as single layers in the same form the wall prints would be for production. Each test weld bead is 100mm long, and double beaded tests were 3mm wide.

For the full-scale deposition prints, 200mm in length, with a 3mm center-to-center bead distance, was used. Based on measurements from the initial testing, the layer height increment was set at 2.5mm. This was subsequently lowered to 2.25mm on later prints when a better average height was determined. Wire sickout was set at 10mm. Pulse DCEP welding current was used. The other specific settings, Trim and Ultimate Arc, were not changed from their standard midpoints. The only setting adjusted was the work point, which drives the WFS and adjusts current and voltage automatically as dependent variables.

The orientation and direction of deposition layer by layer is an important design decision in preparation for additive manufacturing (Lin, et al. 2019). A two-weld bead design is ideal because it creates enough material width for various mechanical tests; while also adding support to the structure, because single bead walls can be challenging to keep maintain in height as build layers increase. The support is necessary to decrease distortion from the high thermal input; to further minimize heat warpage, the direction of each deposition layer is reversed. The overall rectangular shape of the print profile is formed in a U shape that is deposited in the opposite orientation of every layer. Each odd-numbered layer is deposited A-B-C-D, and each even-numbered layer is reversed, depositing B-A-D-C.

Figure 11: Robotic Tool Path for double bead wall

Once the deposition is completed, the manufactured part can be cut from the plate. The substrates used for the manufacturing process were ½” thick 1018 steel plates, 1ft^2 in size, clamped to the table for welding, and remained clamped until the part had sufficiently cooled. Proper clamping and cooling were imperative to minimize warpage in print and to keep the piece in a consistent ‘as produced’ state for the analysis, the thickness of the plate also aided in the minimization of warpage.

3.4 Waveform Study

A waveform study of the different modes was conducted to compare various parameter control methods allowed by the welder. The welding modes tested were Power Mode®, Pulse Mode®, Constant Voltage, and Rapid Arc®. The waveform graphs are generated by Lincolns Power Wave Manager software that directly interfaces with the welder through ethernet. It allows the complete setup of the welder, such as calibration tests, operational control of the welder, settings, and mode adjustments, which in our case are input by the Kuka controller.

Power Wave Manager also allows recording and showing real-time data access via the Weldview and Observer functionality. The observer function is a low-frequency monitoring process that will record significant events, such as welder errors, wire jams, and arc failures, but does not provide detailed data, only sampling at a rate equaling about 4Hz. However, it does offer a relative average amperage and voltage, the constant wire feed speed, and true energy or input energy for the weld. The Weldview traces are manually set to record the amperage and voltage between arc-on and arc-off commands, extending to a full weld or deposition layer. The data is captured at a high sampling frequency of 1200Hz.

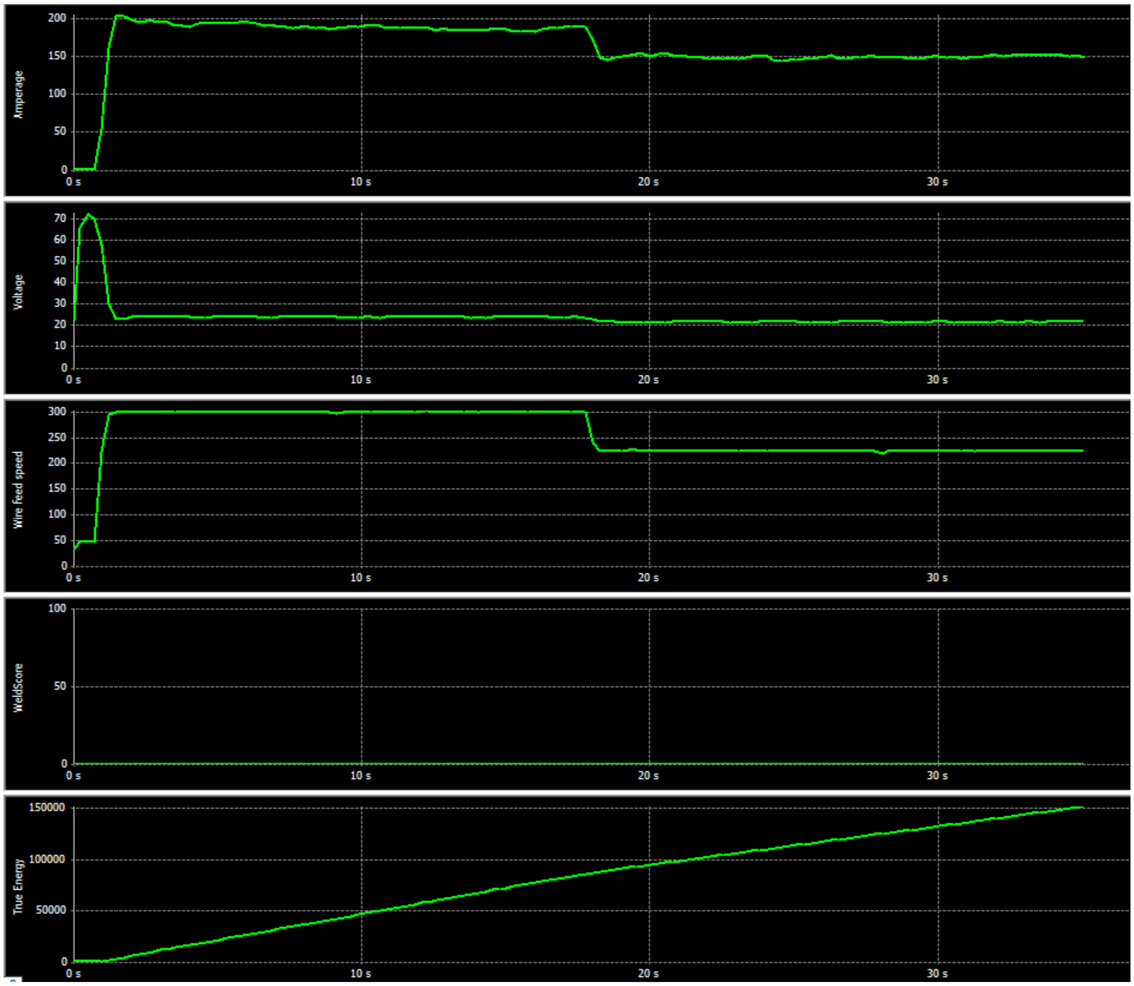

Figure 12: Lincoln Powerwave observer data. Arc ignition peak, 300 work point weld for ~17sec, decreased to 250 work point for the remaining ~17sec

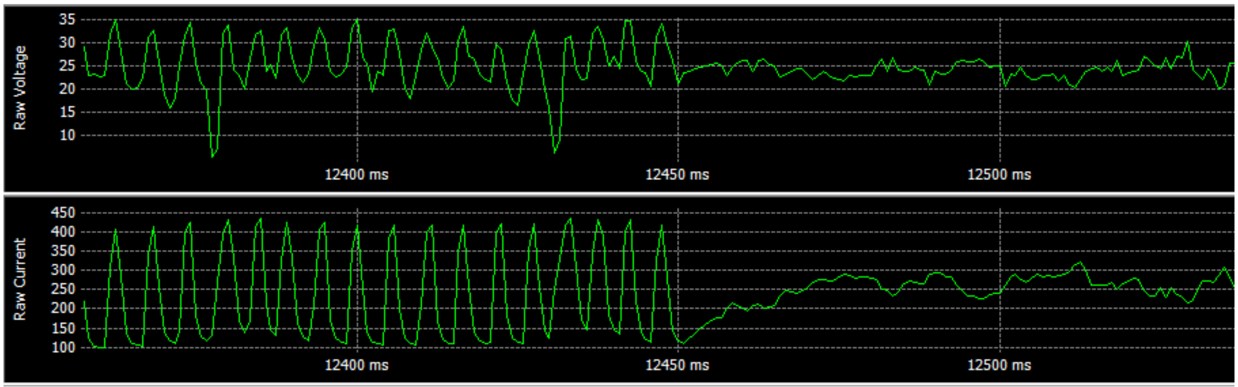

Figure 13: Lincoln Weldview trace graph. With a macro view of pulse mode on the left, and constant voltage mode the right

3.5 Shielding Gas Study

Shielding gas in MIG welding can vary in some instances depending on process and material; the most common is C25, or 75% Ar mixed with 25% CO2; some applications call for the use of other mixtures that may include Helium or Oxygen. The tested mixtures were C25, Pure 100% Argon, 2-3% nitrogen/98% Argon, and 90% Helium/7.5% Argon/2.5% CO2. These are more commonly used gasses and were readily available to use. C25 being the most common was initially selected to be used as the shielding gas. However, early testing showed a large amount of spatter produced from the weld, which is less preferable as it decreases deposition efficiency. To combat the prevalence of spatter, other shielding gasses were tested. The CO2 in C25 is considered an active gas in arc welding, to decrease the presence of active gasses may make the arc reaction more stable. Trimix composed of 90% Helium/7.5% Argon/2.5% CO2 was selected due to its availability as a commonly used TIG welding gas. Still, it possesses other benefits, such as higher ionization energy that may affect the process.

The use of 100% Argon is generally only used in TIG welding and is also readily available; pure Argon is completely inert and therefore shouldn't interact with the weld. This potential was of specific interest to the potential process improvements. In addition to pure Argon, low percentages of nitrogen were mixed into otherwise pure argon shielding gas in previous studies. This addition resulted in improved surface finish, appearance, and smoothness, which would benefit the final matching and processing of the net shape parts would be subject before our testing and real-world use, so for that reason, it was also selected to test (Silwal, Nycz, and Noakes 2018).

3.6 Interpass temp

The temperature of the interpass weld samples was measured at the center of the deposition path. The micro-epsilon CTLM3H2SF300-C3 infrared temperature sensor was used to measure the heat of the part. It has an optical resolution of 300:1, an emissivity of 0.8, and is limited to reading between 200ºC and 1500ºC. The upper limit creates a plateau in the graph as the arc passes through its measurement point. This is not of concern since the cooling curve of 600ºC to 200ºC is within this range and the primary examination window. Determining the rate at which the part cools between 600ºC to 200ºC is important for the interpass temperature and the interpass temperature and cooling curves.

Four testing welds were performed for interpass analysis, a single layer pretest, a 'run time delayed' two-layer sample, a 'double delay' two-layer sample, and a temperature-dependent two-layer sample. Each weld performed was performed to the same size and speed as the large-scale tests, with no other changes. The single-layer baseline test was a weld performed ABCD along the established path with no second layer. The ‘run time’ test was performed as programmed with no wait states in the robot movement, the delay between arcs is from the movement time between the fits layer’s endpoint D and the second layer start point B, which equates to 20 seconds. The ‘double delay’ test was performed with an extra delay between points D and B, doubling the initial time to 40S. The third test was not time-based; instead, it was temperature dependent. Once the previously deposited layer reached 300ºC, the program was resumed, and the arc was struck again for the second deposition layer to begin.

3.7 RAFM wire

The RAFM metal-cored wire alloy specifications were designed by following multiple literature review sources and the functional capabilities of the wire producer, Polymet USA. The chemistry selection was heavily influenced by Tungsten and Tantalum alloy components tested at varying levels (Laha et al. 2013). The alloy elements' weight percent of the wire was tested after its production to confirm the composition was within the acceptable ranges.

Table 2: RAFM wire alloying composition in experimental wire

RAFM Alloying Material Composition, by weight %					
Cr	8.84	W	1.2	C	0.10
Mn	0.40	Ta	0.06	Ti	0.012
V	0.02	Cu	0.028	S	0.012
Al	0.017	Mo	0.014	P	0.011
Co	0.006	Ni	0.02	Co	0.006
Si	0.042	B	<0.001	Nb	<0.001

3.8 Material Science Processing

Each microstructure sample was cut in a vertical orientation from the manufactured wall with a liquid cooled abrasive saw to prepare. These samples are pressed into a thermoplastic puck for sanding and polishing purposes. That process requires the sample to be ~20mm across or less to fit into the mold. The larger prints were also cut horizontally into smaller sections so they could be molded. The pucks with the surrounded sample are then sanded and polished. The sanding process is a wet process throughout and begins with a rough 80 grit to ensure the sample is flat and then successively moves to finer grits; 120, 240, 400, 800, and 1200 grit are used. After which point, the sample is cleaned and dried; the polishing process can begin. The sample is then polished to remove any remaining scratches. The polishing process uses alumina silicate to lubricate the pad and aid with polishing. After which, the sample is rinsed and air-dried.

For the etching process, several options exist; using the ASTM E407-07(2015) standard, one of the recommended stainless steel and chromium alloyed steel etchants is oxalic acid in conjunction with an electrolytic process. The added benefit of the electrolytic process was appealing because initial attempts to etch the samples with 4% Nital solution were unsuccessful. Based on formula 13 of the ASTM standard, a 10% oxalic acid solution was used in conjunction with an electrolytic process. A power supply was used to supply a constant 8 volts, higher than the recommended 6V, with the cathode placed in the solution and the anode placed in contact with the face of the submerged sample. The reaction was immediately noticeable; however, the timeframe was longer than expected, the recommended being below 60 seconds when the process took 5 to 6 minutes to achieve a strong etch in this instance (Eftink, et al. 2021). After the raw etching was completed, the samples were rinsed and placed into an ultrasonic cleaner for

2.5 mins each to clean and remove any remaining debris. After which, the samples were rinsed with isopropyl alcohol to remove any moisture from the surface and prevent oxidation. Once the preparation was complete optical microscope pictures were taken, and further testing could begin. The variation in layers can be seen clearly after the etching process.

3.9 Mechanical Testing

Hardness testing of materials is a very common mechanical test; HRC hardness and HV microhardness were performed on various deposited samples. The HRC hardness was used to establish a baseline of the deposited metal's general hardness. This can help to indicate if the expected phases are present but do not tell the whole story. HRC hardness indentions were performed to try and determine if there was any recrystallization happening on the earlier deposition layers relative to the freshest layers. Microhardness was conducted across the height of the deposited material to map any changes in hardness throughout the layers. If a significant hardness variation was observed in any location across the sample, that would indicate some form of recrystallization or tempering has occurred during the deposition process.

The strongest point of interest with hardness testing is to determine the presence of grain reformation. As the part is heated and cycled on each deposition pass, it is unknown what the resulting grain sizes will be and how the phases will be affected. The older martensite may become tempered to a lower hardness when compared to the freshly deposited layers. There is also a further possibility that some of the martensite is being reformed into austenite or δ-ferrite.

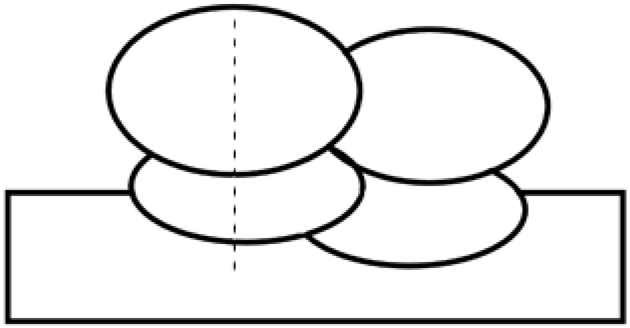

Figure 14: Microhardness test pattern along height of sample

Impact Toughness testing was designed according to ASTMA370; a total of eight sub-size Charpy impact V-notch specimens (5×5×25mm) were prepared. The cuts were sectioned horizontally along with the deposited layers; no vertical test specimens were cut. The tests were then conducted at six temperatures to try to determine where the materials DBTT may be present. The Ductile to Brittle Transition Temperature is the point at which the material's ability to absorb impact energy is greatly reduced due to temperature, causing the failure mode to transition from ductile to brittle; this is valuable information to know for the possible use case recommendations of the material. The testing temperatures selected are 0, 25, 50, 100, 150, and 200 degrees Celsius because high hardness steels can fail in a brittle manner even at temperatures above 0ºC.

CHAPTER 4: RESULTS

4.1 WAAM attempts

First welding trials began with near no baseline. The travel speed was 14mm/s, and the wire feed speed was set to 375 in/min. Most of the weld modes used were synergic, meaning with the set wire feed speed called the “work point,” the power is automatically adjusted to match. The pulsed current measured minimum amperage of 120A and a peak amperage of 375A; the wire feed speed and peak amperage pulse were directly correlated with the work point. Pulse current was the initial testing priority for its decrease in overall heat input and increase in peak amperage, lower heat assists in mitigating warpage. Higher peak amperage should be changing the metal transfer method to spray transfer. Two beads of each weld type and setting parameter were deposited, with the pulse mode modifiers R5-R7 only a single pass.

Table 3: Weld bead naming correlation to shielding gas

R =	25/75 CO_2/Ar
A =	100% Ar
T =	Tri-mix He/CO_2/Ar
N =	2.1%-N2/AR

Figure 15: R1 - R7 Weld Mode Trials

Table 4: R1 - R7 Weld mode parameters

Weld #	R1	R2	R3	R4	R5	R6	R7
Bead type	Single	Single	Single	Single	Single	Single	Single
Speed (mm/s)	14	14	14	14	14	14	14
Mode	power mode	Constant Voltage	Rapid arc	Pules	Pulse	Pulse	Pulse
Power level	3.5kW	18V					
WFS (in/m)	225	400	430	375	375	375	375
Trim	-	-	1	1	1.25	0.75	1
Ultimate Arc	-	-	0	0	0	0	-5
Wire Stick out (mm)	10	10	10	10	10	10	10
bead width avg (mm)	5.00	5.64	8.28	7.67	10.77	6.08	7.60
bead height avg (mm)	3.20	5.04	5.62	3.04	2.91	4.37	3.69
Gas flow rate (L/m)	17	17	17	17	17	17	17
Notes	non synergistic	-	-	-	longer arc	shorter arc	lower frequency

Figure 16: R8 – R11 Weld Mode Trials

Table 5: R8 – R11 Weld mode parameters

Weld #	R8	R9	R10	R11
Bead type	Single	Single	Double	Double
Speed (mm/s)	8.32	8.32	14	14
Mode	Pulse	Pulse	Pulse	Constant Voltage
Power level	-	-	-	18V
WFS (in/m)	375	375	375	400
Trim	1	1	1	-
Ultimate Arc	0	0	0	-
Wire Stick out (mm)	10	10	10	10
bead width avg (mm)	7.07	5.12	11.96	9.05
bead height avg (mm)	2.99	4.76	3.62	4.65
Gas flow rate (L/m)	17	17	17	17

Figure 17: A1 – T3 Weld Mode Trials

Table 6: R1 - R7 Weld mode parameters

Weld #	A1	T1	T2	T3
Bead type	Single	Single	Single	Single
Speed (mm/s)	14	14	14	14
Mode	Pulse	Pulse	Pulse	Pulse
Power level	-	-	-	-
WFS (in/m)	225	300	225	375
Trim	1	1	1	1
Ultimate Arc	0	0	0	0
Wire Stick out (mm)	10	10	10	10
bead width avg (mm)	4.73	5.57	4.45	6.25
bead height avg (mm)	2.70	2.86	2.81	3.61
Gas flow rate (L/m)	17	18	18	18

Figure 18: T1 – N4 Weld Mode Trials

Table 7: T5 – N4 Weld mode parameters

Weld #	T5	T6	T7	T8	N2	N3	N4
Bead type	Double	Double	Double	Double	Double	Double	Double
Speed (mm/s)	14	14	14	14	14	14	14
Mode	Pulse	Pulse	Pulse	Pulse	Pulse	Pulse	Pulse
Power level	-	-	-	-	-	-	-
WFS (in/m)	300	225	225	225	225	225	300
Trim	1	1	1	1	1	1	1
Ultimate Arc	0	0	0	0	0	0	0
Wire Stick out (mm)	10	6	6	10	10	10	10
bead width avg (mm)	9.95	8.48	9.82	9.30	6.65	8.41	8.99
bead height avg (mm)	3.51	2.95	2.46	2.71	4.18	3.34	4.74
Gas flow rate (L/m)	18	18	18	18	11.54	11.54	11.54
Notes	-	-	5mm bead separation	4mm bead separation	-	4mm bead separation	4mm bead separation

4.2 Waveform Study

The waveforms of the previous tests were all graphed and recorded with the power wave manager trace function; this high frequency sampled data allows for the current analysis. One of the main focuses is arc stability; the observed consistency of the pulse mode welds was greater than that of the constant voltage and power mode welds. Arc instability was a concern due to the frequency of wire burn errors during initial testing; it was believed these issues might amplify as the deposition layers increased and surface uniformity decreased.

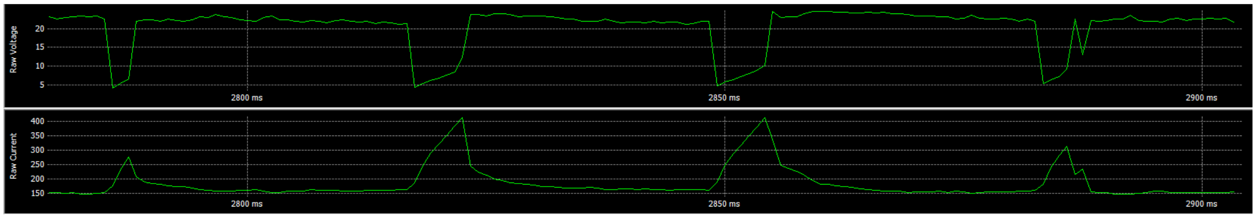

Figure 19: R1 voltage and amperage wave form

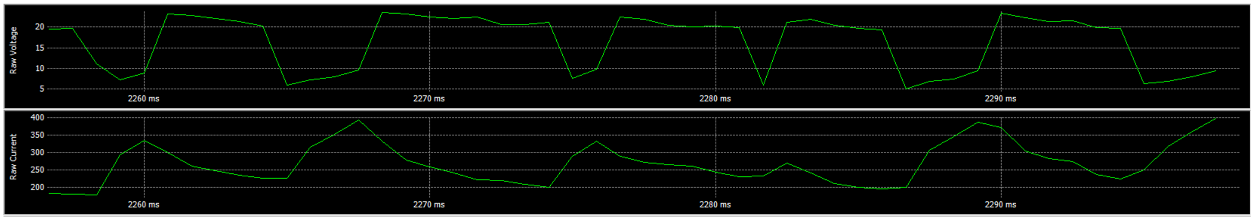

Figure 20: R2 voltage and amperage wave form

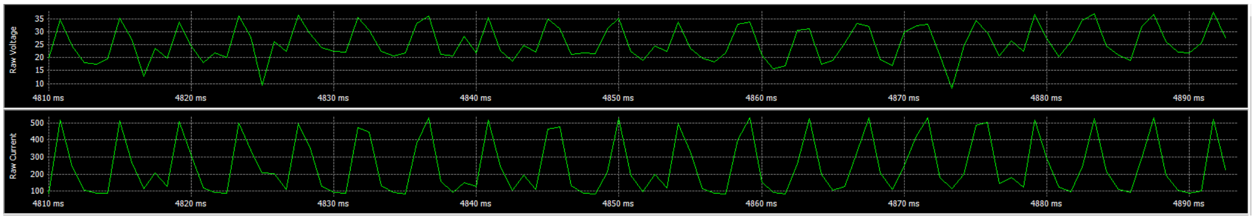

Figure 21: R3 voltage and amperage wave form

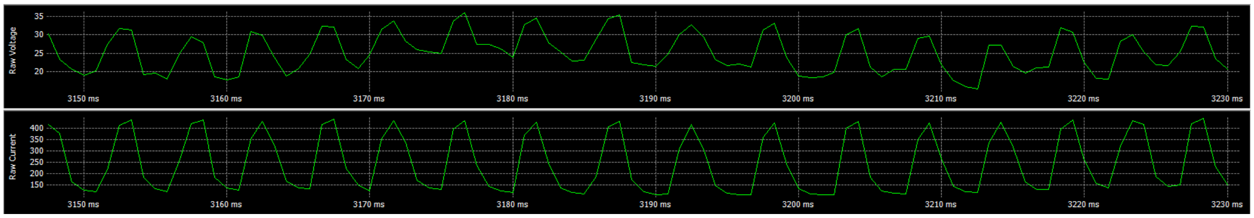

Figure 22: R10 voltage and amperage wave form

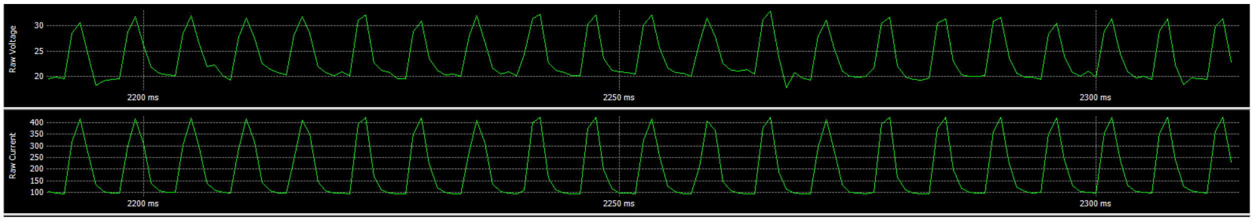

Figure 23: A1 voltage and amperage wave form

Figure 24: T1 voltage and amperage wave form

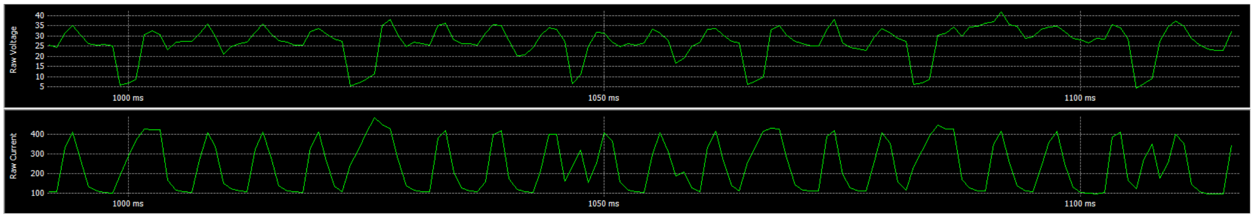

Figure 25: N3 voltage and amperage wave form

Figure 26: R11 voltage and amperage wave form in micro scale

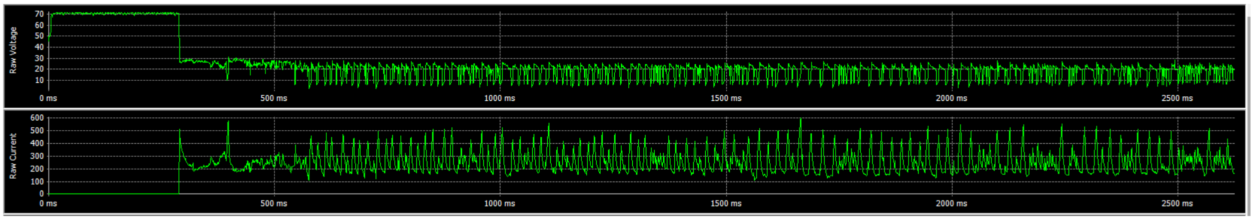

Figure 27: R11 voltage and amperage wave form in a macro scale, showing arc start

4.3 Arc Welding Deposition

The initial large-scale prints reached 4.5 layers and 12.25 layers in height. The endpoints were the arc failures during the deposition process, not the programmed endpoints. Heat buildup in the part and primarily in the air-cooled torch became a continual issue with the deposition continuity, which necessitated taking the longest breaks in-between layer prints possible. This necessity initiated the interpass temperature study to determine if the intermittent cooling time had a noticeable effect on the phase structure as it was a further step of the directional heat cycling.

Figure 28: Double Bead wall test, 375WP, excess heat buildup, end geometry failure

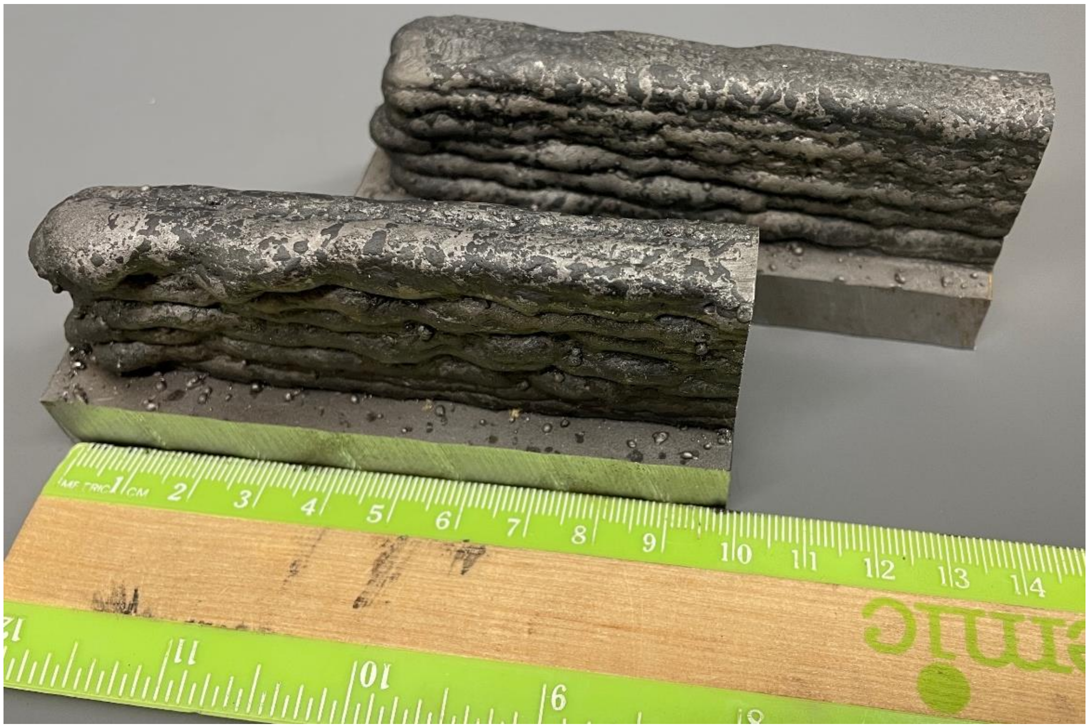

Figure 29: Double Bead wall test, 375WP cleaned and cut to be used for impact testing

Figure 30: double bead deposition wall, 300WP, 115mm peak height, 56-layer

Deposition losses can be seen in the amount of spatter surrounding the wall and the drips on the edges from where the heat buildup caused drops of metal to fall off the ends of the wall. This was the best possible result as other scenarios suffered far worse geometric instability and the largest print that was successfully conducted. This sample was waterjet in preparation for destructive testing as a tensile test; however, it was found to have too much porosity and would most likely fail prematurely due to the overwhelming presence of these possible stress concentrations. The significant presence of porosities found in the wall print was a driving factor in exploring the use of other shielding gasses to decrease their prevalence in future prints. Ideally, the deposited material would be completely solid and free of any voids that may affect its mechanical properties.

Figure 31: 56 layer double bead wall, waterjet into wishbone tensile coupons

In Figure 31, the presence of porosity can be observed on most of the sides of the tensile coupon cross-sections. These samples were cut from the wall in Figure 30. Due to this abundance of priority, no tensile test was conducted as they would have introduced stress concentrations into the trials, which would have provided data not indicative of the true strength of the material, and thus no sound conclusions could have been drawn from the findings.

The Figures in Appendix A, show the code written by hand for the mid to large-scale wall prints. This code worked as a loop to increment a standard height increase onto the rectangular shape wall pattern, pictured in Figure 9. The code declares local position variables as the incremented positions and has a Z height offset variable for changing the deposition layer height. Each for loop is two opposite direction deposition layers with arc commands, and Z height increases after each deposition pass. The first command group acts as a trace to the welded points and allows for rapid updating of the locations. The initial points set as XP1, 2, 3, and 4 are then copied to the newposition1, 2, 3, and 4 variables so the latter can be overwritten without changing the former points globally. The loop runs three times, or six layers, after which it moves to a service position where the torch can be cleaned of spatter.

4.4 Interpass Temperature Tests

When the interpass temperature test began when the print tests showed an increased arc failure rate, the problem was identified to be heat buildup in the torch, which is air-cooled, to combat this, wait times in-between welds were introduced. The effect on the grain structure was essential to understand as any recrystallization will affect the mechanical properties.

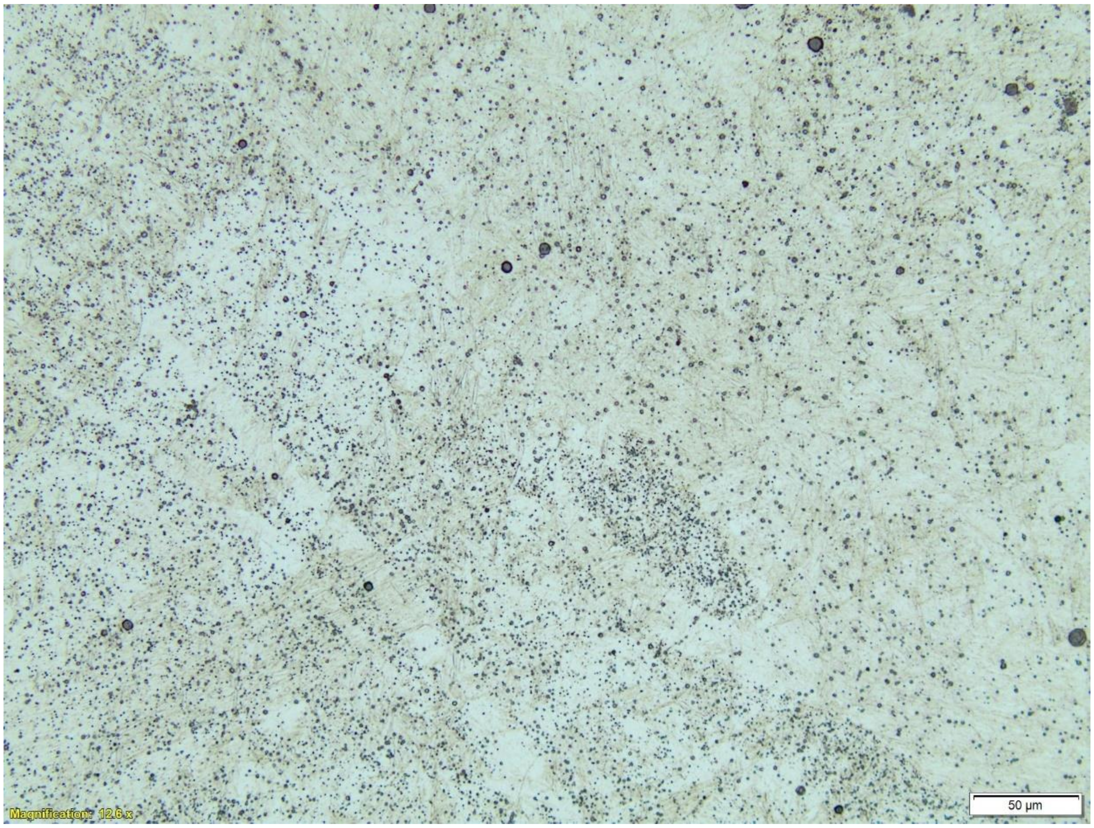

Figure 32: Baseline Single Layer Two Bead Microstructure

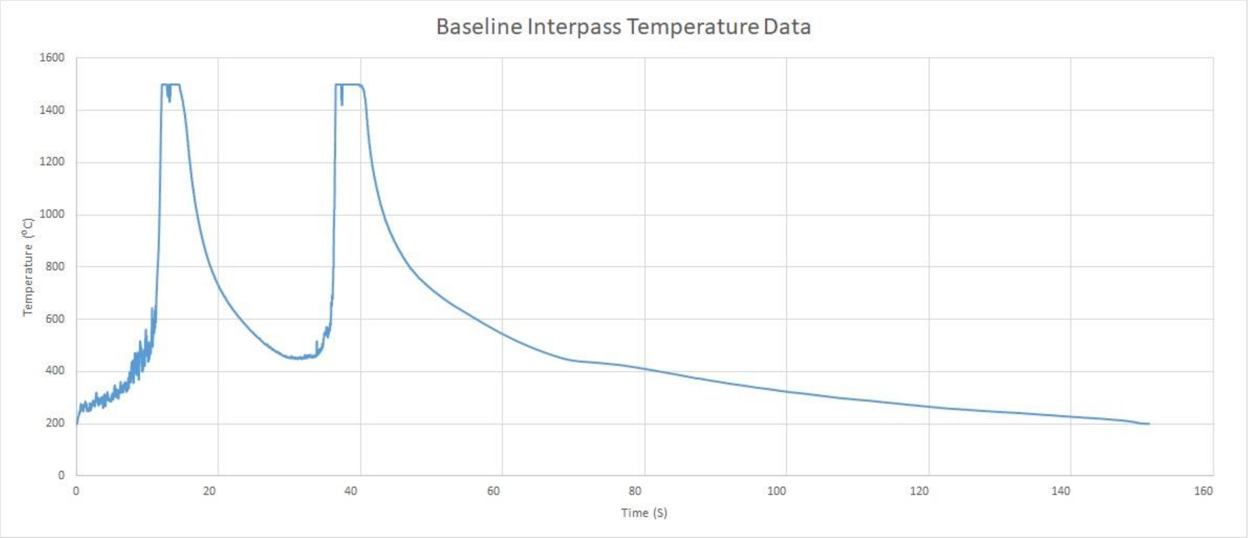

Figure 33: Baseline Single Layer Two Bead Temperature vs. Time Graph

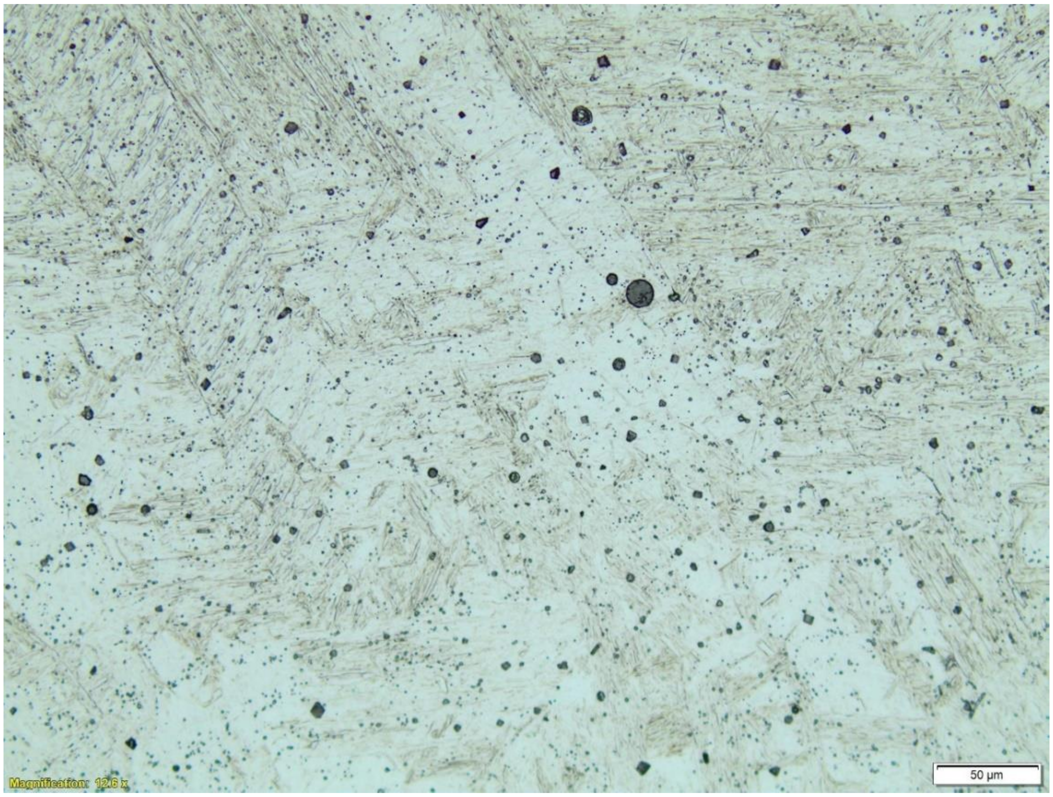

Figure 34: 20 Second Pause Top Layer Two Bead Wall

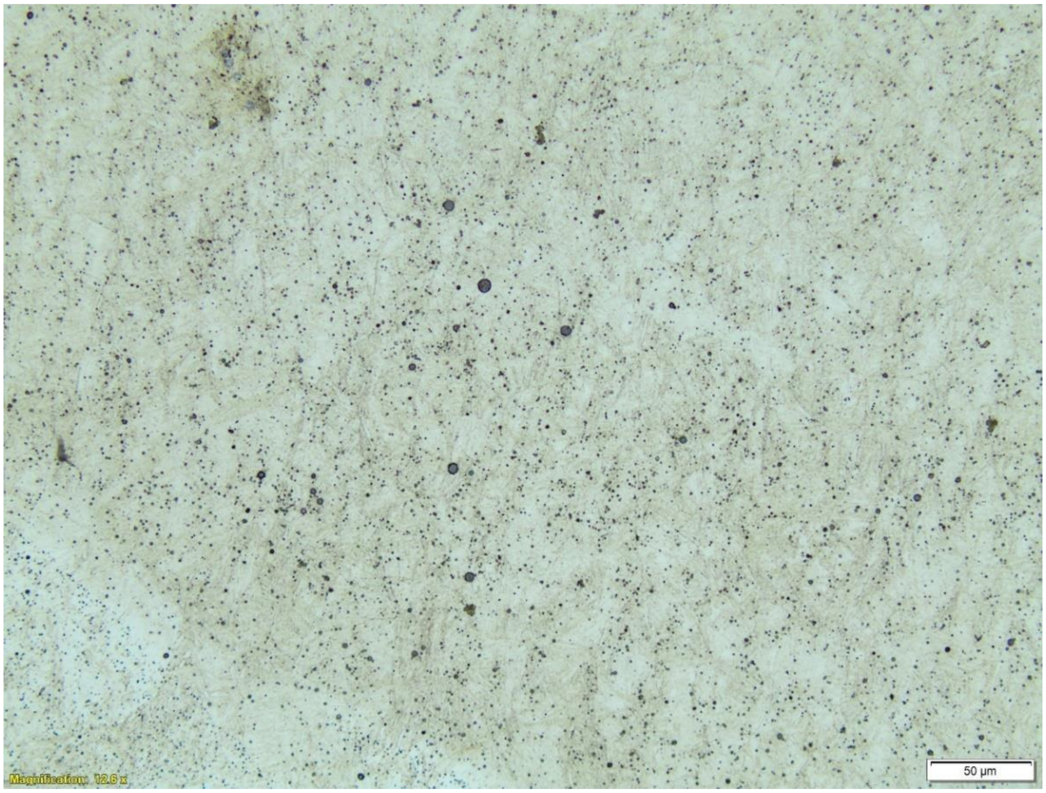

Figure 35: 20 Second Pause Bottom Layer Two Bead Wall

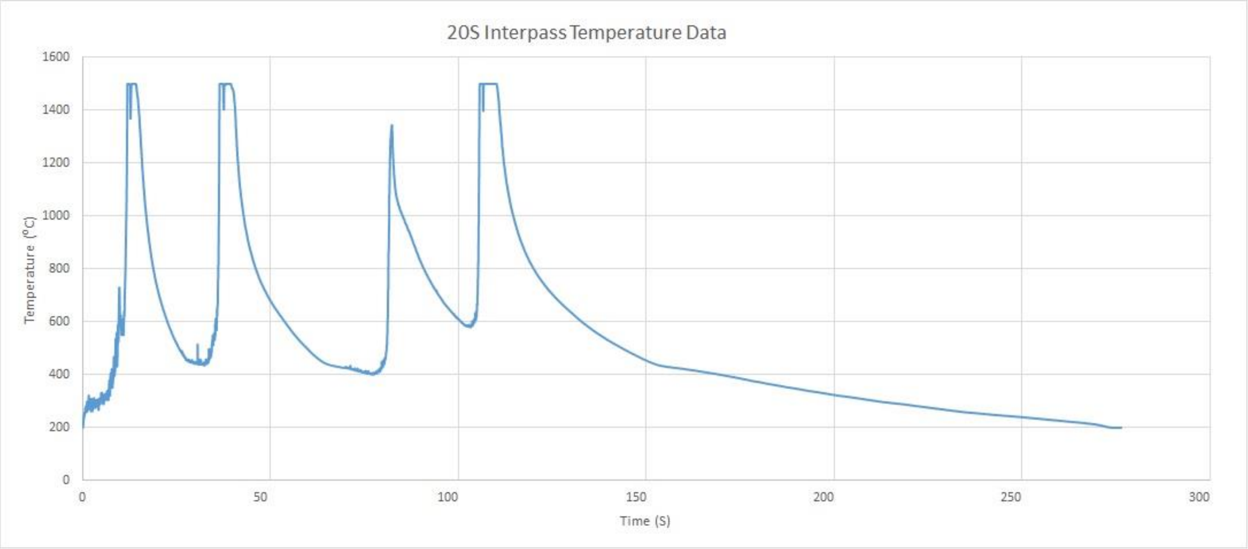

Figure 36: 20 Second Pause Two Bead Temperature vs. Time Graph

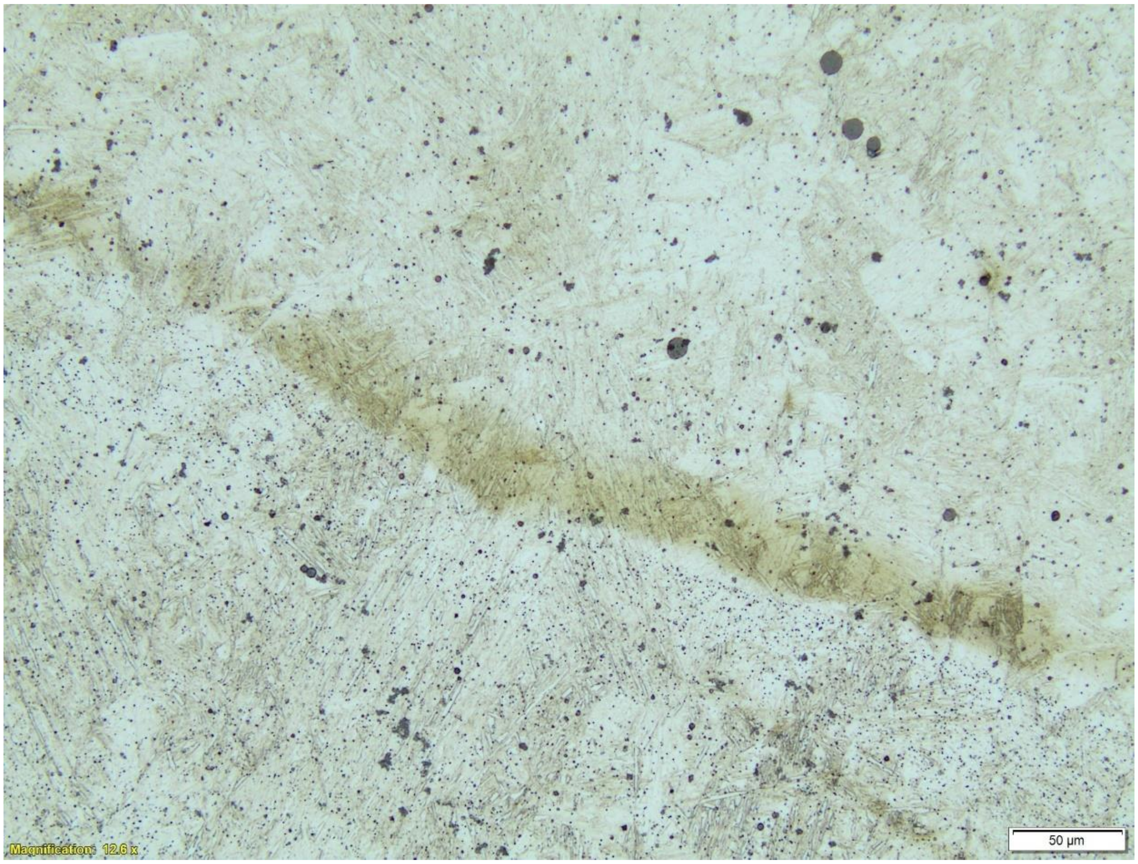

Figure 37: 40 Second Pause Bottom Layer Two Bead Wall

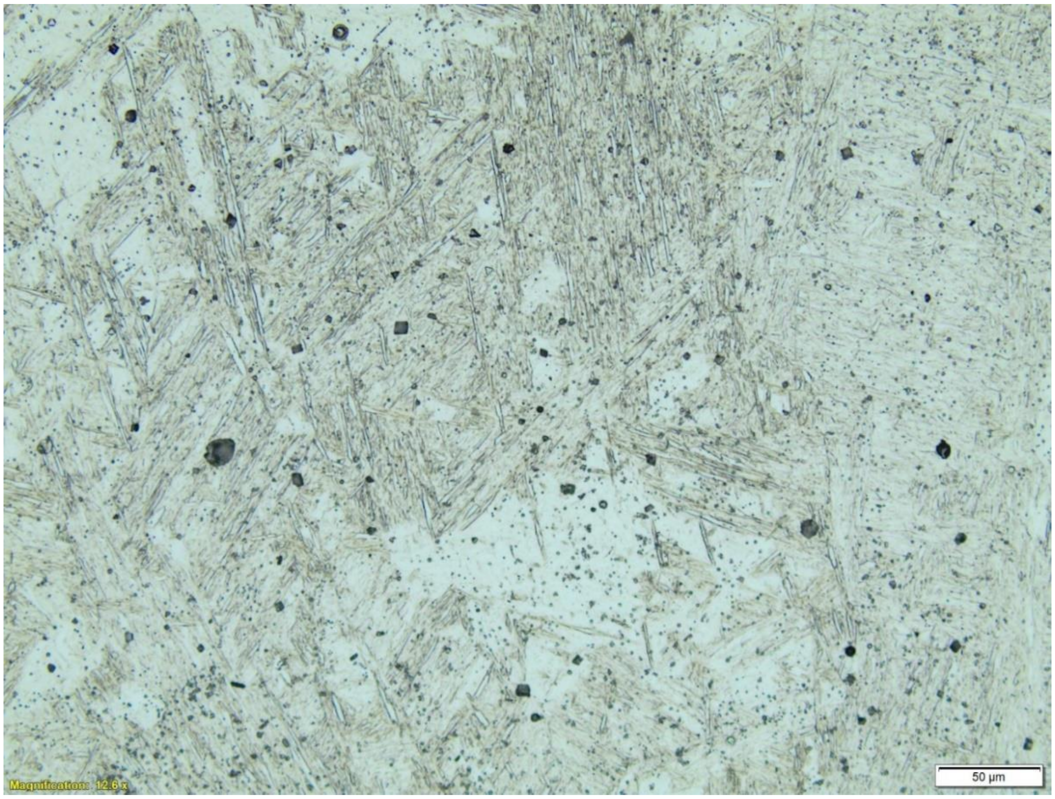

Figure 38: 40 Second Pause Top Layer Two Bead Wall

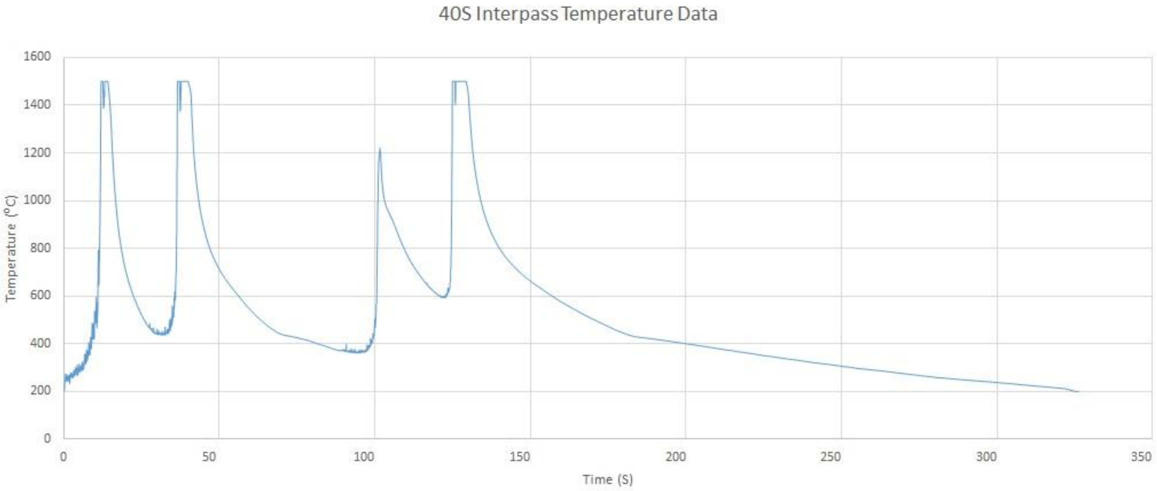

Figure 39: 40 Second Pause Two Bead Temperature vs. Time Graph

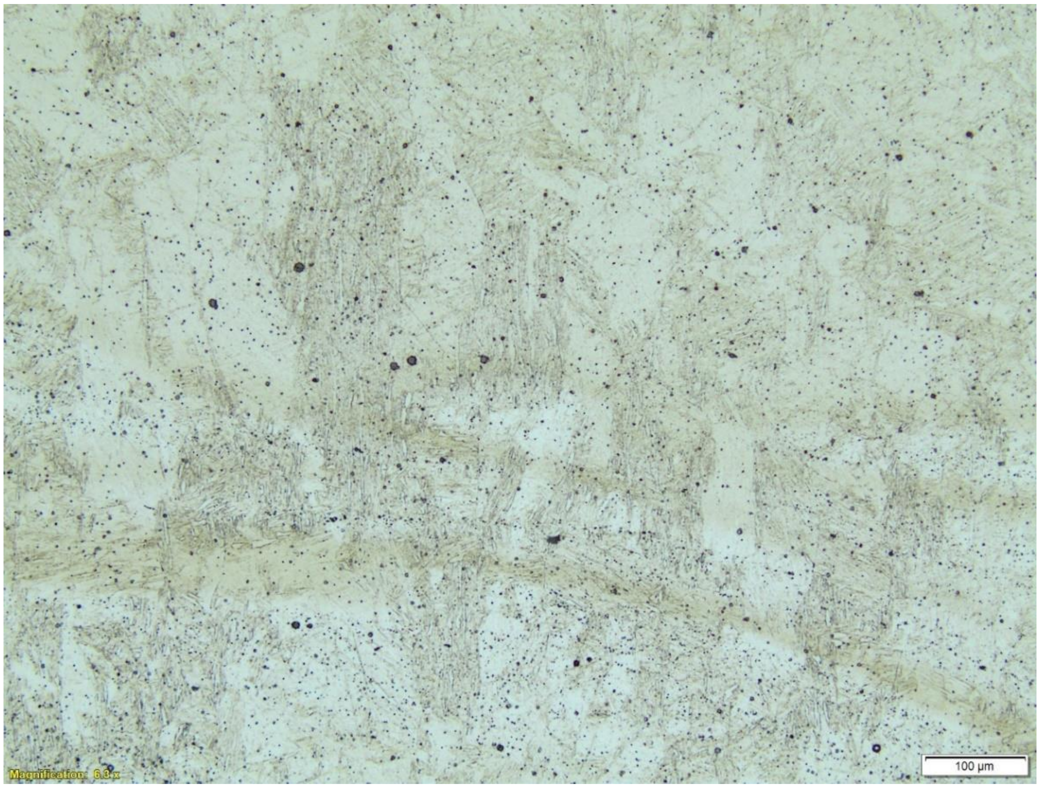

Figure 40: 300ºC Bottom Pause Top Layer Two Bead Wall

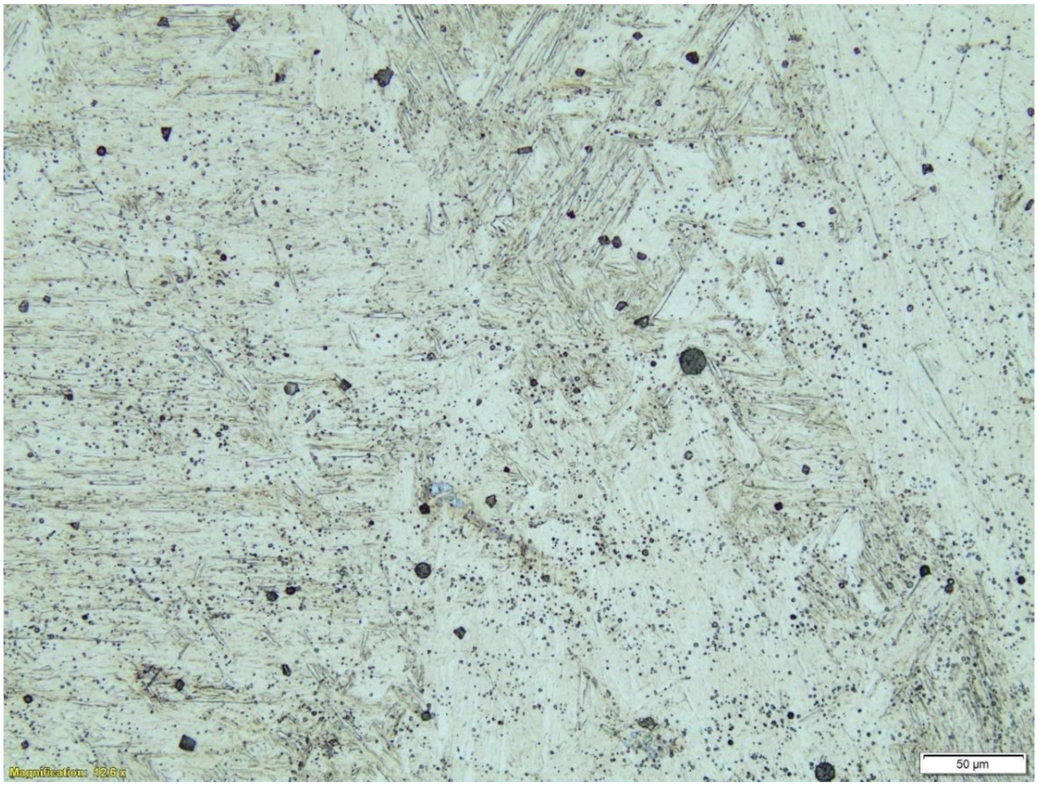

Figure 41: 300ºC Temp Pause Top Layer Two Bead Wall

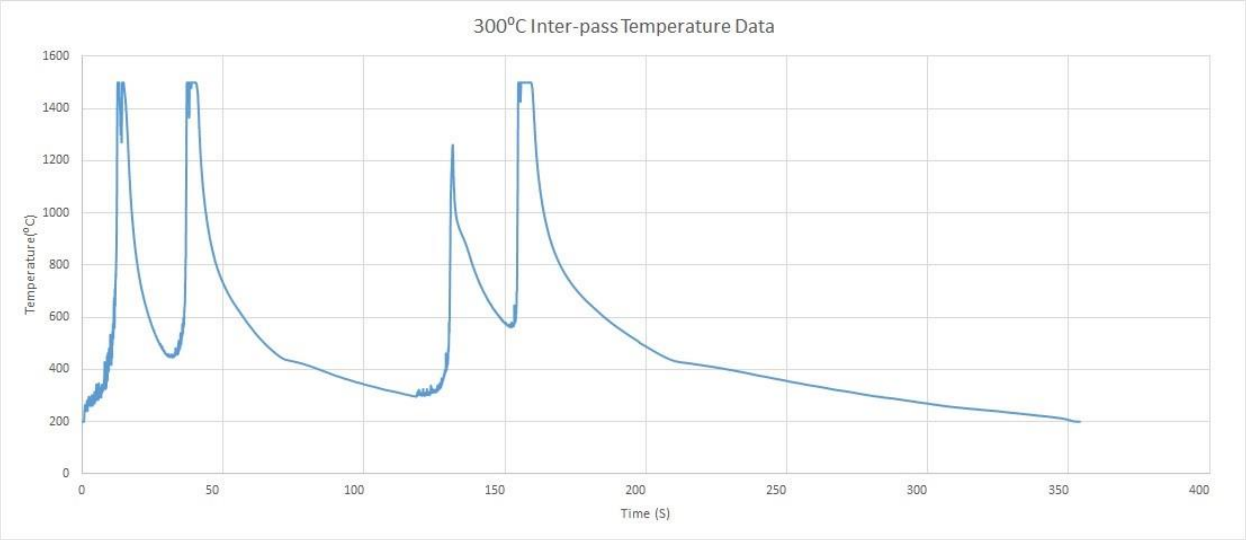

Figure 42: 300ºC Temp Pause Two Bead Temperature vs. Time Graph

The dual peaks in the graphs are formed by the forward and return path of the welder performing a two-bead wall. The temperature was measured from the middle of the print length. The peaks are also plateaued at 1500ºC when the arc is passing across the measuring point exceeding the capabilities of the sensor; this does not affect the data because the critical information is below 500ºC as the deposited material is cooling in-between layers. In Sam, et al. (2014), when examining multipass RAFM welds, the δ-ferrite present in weld metal deposited on the previous pass transforms to austenite during the weld's thermal cycle; this brings down the overall δ-ferrite content in multipass welded parts. We are looking for the formation of the delta ferrite amongst the primarily martensitic structure to determine if tempering is occurring during the deposition and subsequent cooling process.

4.5 Morphology Identification

Examining the microstructure compared to other “as received” or “as cast” samples, from literature, regarding RAMF alloys gives an indication of how well this production method produced the alloy we desired.

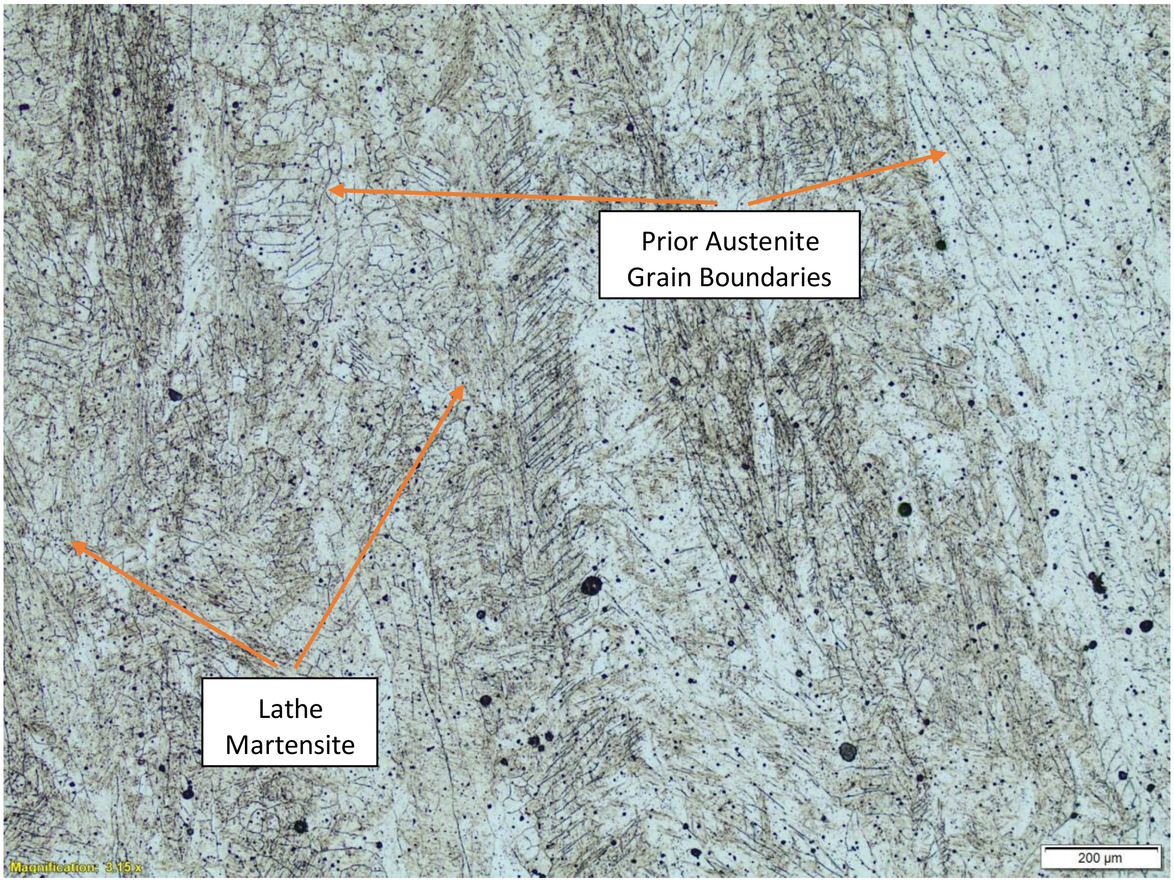

Figure 43: Lathe Martensite formation, and prior austenite grain boundaries

The microstructure mainly consists of lathe martensite, which is expected from low carbon, high hardness steel. There may also be the presence of carbides; some of these carbides may be Tungsten carbides. This observation is interesting because the carbon present may have aided their formation in the C25 shielding gas, which can help to explain the relatively high amount of spatter during the deposition process. There was very little delta ferrite observed, only one instance clearly stuck out in the microscope images shown in Figure 45, but prior austenite grains can be seen in most of the images.

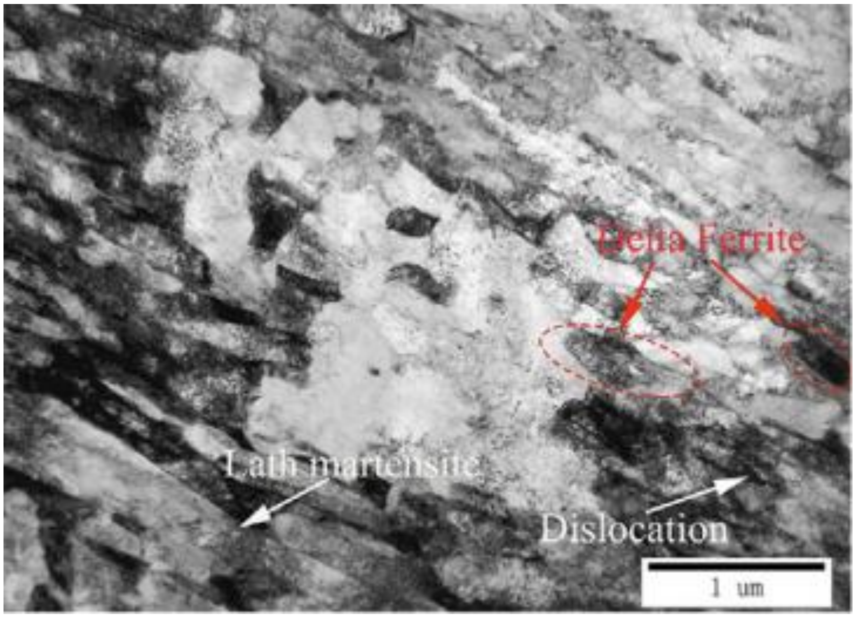

Figure 44: Microstructure of CFL-1 welded joint (S. Wu et al. 2020b)

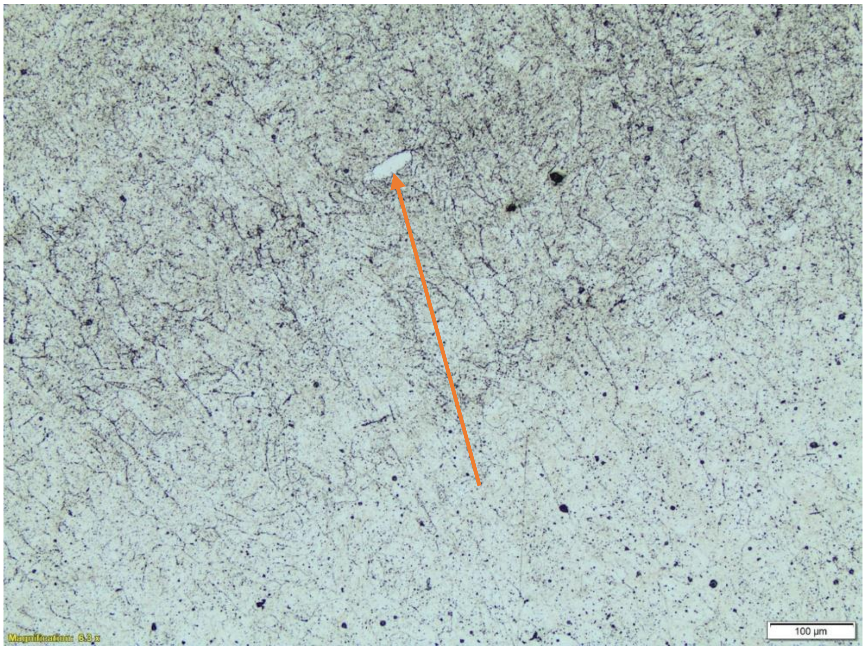

Figure 45: Delta Ferrite formation

4.6 Hardness Testing Analysis

Initial Rockwell hardness testing was performed on the 4.5-layer height sample. Five tests were administered across the surface, at locations shown in Figure 46, for deposition layer in the sample. The HRC standard used to calibrate was labeled 51.78 and measured at 49.1; the test results are adjusted accordingly, averaging just shy of 40HRC with minimal deviation from the median. This was surprising because some form of tempering gradient was expected. However, with the base first and last layers nearly the same hardness, there is no reason to believe the sample has experienced uneven cooling that can affect the microstructure.

Table 8: Rockwell hardness results for 20S multilayer test

Location	1	2	3	4	5	AVG
HRC (calibrated)	40.7	38.2	40.7	40.2	40.1	39.98

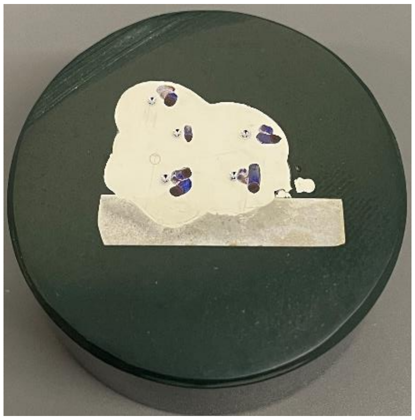

Figure 46: 4.5 Layer Height Wall HRC testing

Further Rockwell hardness testing was conducted on samples deposited after process impartments were made. A sample originally cut for tensile testing was used to perform the secondary hardness testing, these samples were sectioned along the height of the deposited wall. Hardness tests were marked every 1/8th inch, to examine the differences in the deposited layers; this test was conducted on the front and back sides of the section. An additional hardness test was conducted on one side of an unused tensile specimen vertically sectioned from the 56-layer wall deposition. The data can be seen in the Tables located in the Appendix. These test results do not show a continual trend, such as increased hardness with height, that could be correlated with a continual relaxation or reformation of grains during the process. The graphs do show how much the material varies in hardness across the deposition layers, which may indicate that the direction of each deposition layer plays a direct role in the grain size of that material. The sizeable initial drop-off in hardness on the tensile bar was due to a large inclusion.

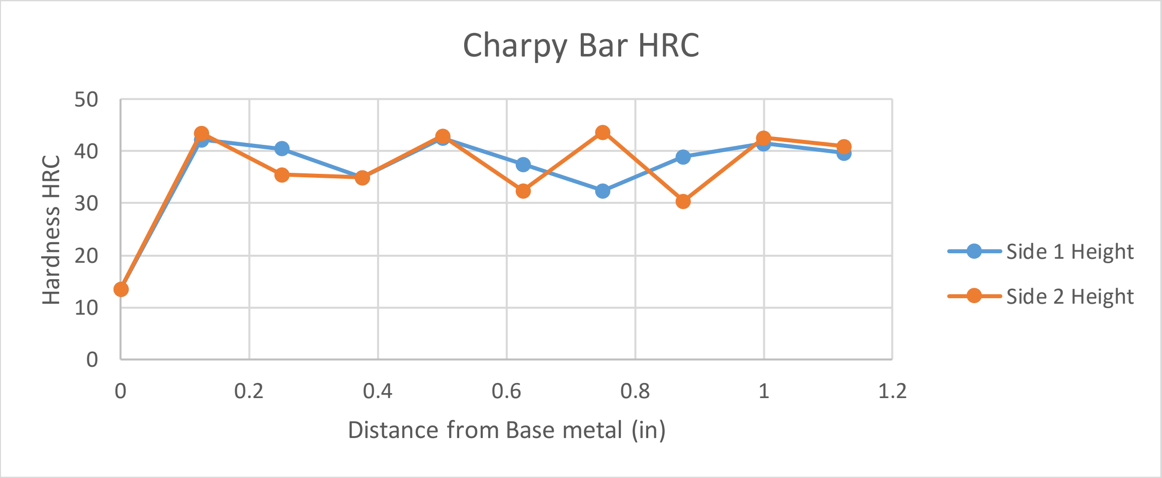

Figure 47: Charpy sample bar HRC hardness testing

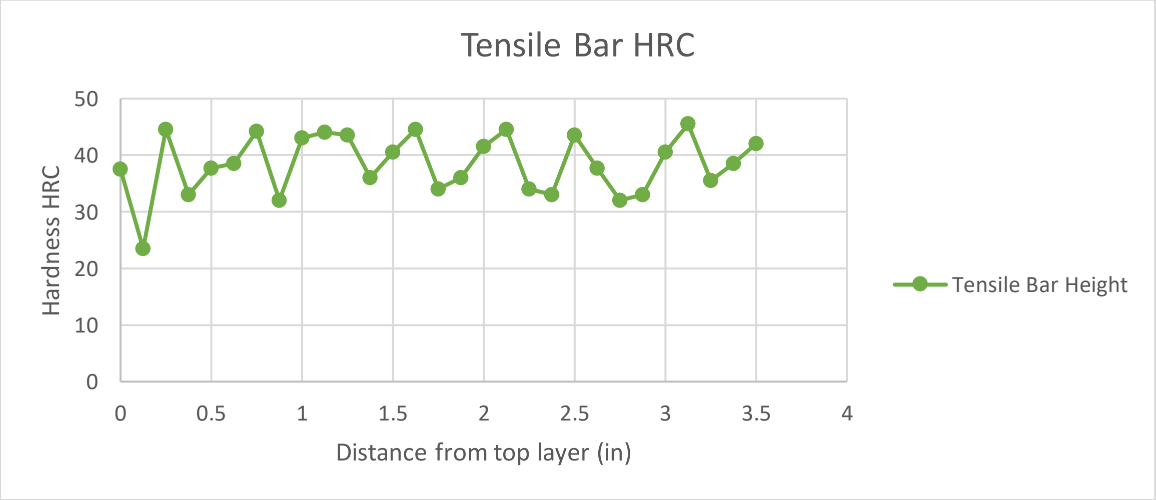

Figure 48: Tensile sample bar HRC hardness testing

Figure 49: Tensile bar HRC hardness test

Microhardness test results of interpass samples were measured in Hardness Vickers. The testing parameters and calculations are shown in Table 9, and the hardness results for each interpass sample tested are shown in the Appendix.

Table 9: Microhardness testing parameters and calculations

Hardness Vickers Testing	Dwell time= 5s
HV = 0.189*(F/d^2)	Force applied = 100gf
F = force applied	d = mean of edge widths

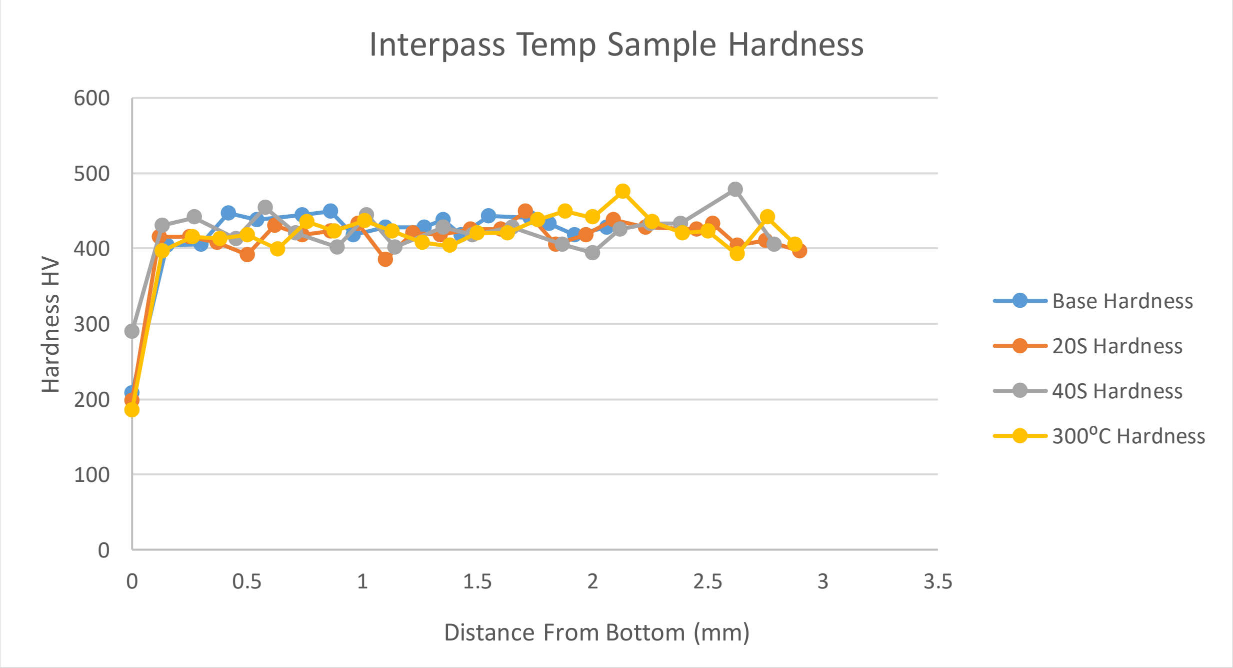

Figure 50: Hardness along the height of interpass samples

The microhardness results are consistent across the height of the specimens; as seen in Figure 50, the possibility of a hardness differential between deposited layers with different interpass temperatures does not seem to be the case. This means any changes in the material's microstructure are minimal and unlikely to affect the mechanical properties in this trial. The low initial hardness displayed on the graph is due to the first measurement point being the interface of the 1018 base metal below the deposited RAFM material being measured.

4.7 Impact Toughness

The impact testing specimens were cut from a 375WP double bead wall that measured 12.25 layers high. The print was faced and decked in a CNC mill to ensure flatness, after which the sample was placed in wire EDM to cut specimen sizes. For the final tolerancing, each sample was face ground for uniformity.

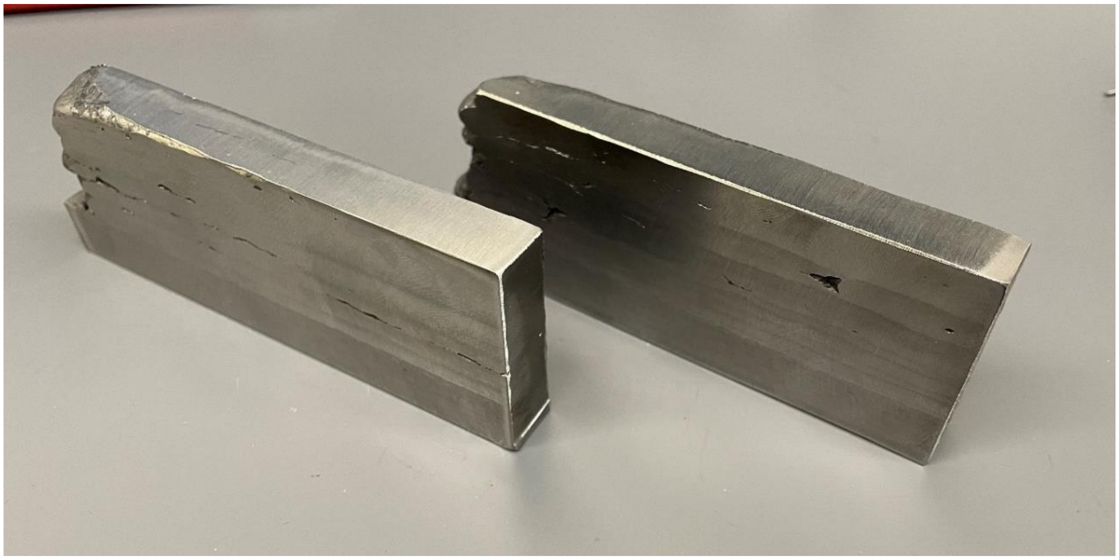

Figure 51: Double Bead wall test, 375WP CNC milled flat

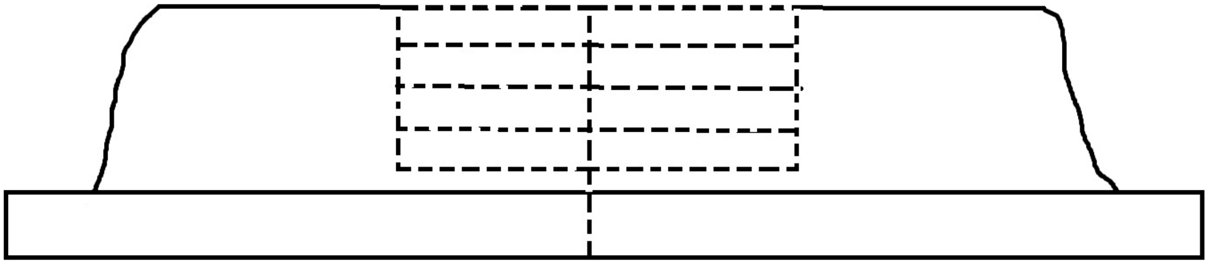

Figure 52: Charpy test sample sectioning

Deep porosities are shown on the surface from a lack of refusion between deposition layers at the edges; some porosities are visibly deeper in the sides and can be seen in the section cut. Once the cutting and grinding were complete, these surface porosities were not of concern. The internal and concealed ones could affect the impact toughness measurements. Still, since that is the as produced quality of the material with current process development, that is how it would fail in a service application as well. The notch cut into the specimen for testing purposes should create a more significant stress concentration than any porosity present. No failure was recorded at a different location where the notch was cut.

Table 10: Charpy test results performed at Oakridge National Lab, tested to ASTM A370

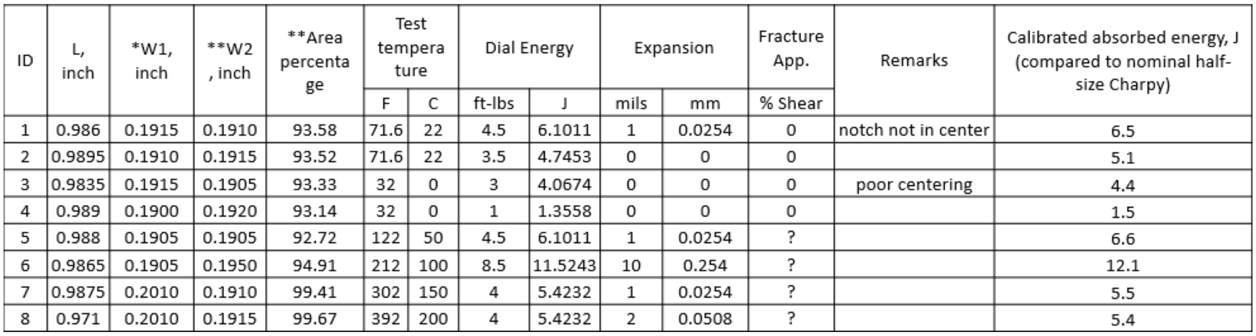

ID	L, inch	*W1, inch	**W2, inch	**Area percentage	Test temperature		Dial Energy		Expansion		Fracture App.	Remarks	Calibrated absorbed energy, J (compared to nominal half-size Charpy)
					F	C	ft-lbs	J	mils	mm	% Shear		
1	0.986	0.1915	0.1910	93.58	71.6	22	4.5	6.1011	1	0.0254	0	notch not in center	6.5
2	0.9895	0.1910	0.1915	93.52	71.6	22	3.5	4.7453	0	0	0		5.1
3	0.9835	0.1915	0.1905	93.33	32	0	3	4.0674	0	0	0	poor centering	4.4
4	0.989	0.1900	0.1920	93.14	32	0	1	1.3558	0	0	0		1.5
5	0.988	0.1905	0.1905	92.72	122	50	4.5	6.1011	1	0.0254	?		6.6
6	0.9865	0.1905	0.1950	94.91	212	100	8.5	11.5243	10	0.254	?		12.1
7	0.9875	0.2010	0.1910	99.41	302	150	4	5.4232	1	0.0254	?		5.5
8	0.971	0.2010	0.1915	99.67	392	200	4	5.4232	2	0.0508	?		5.4

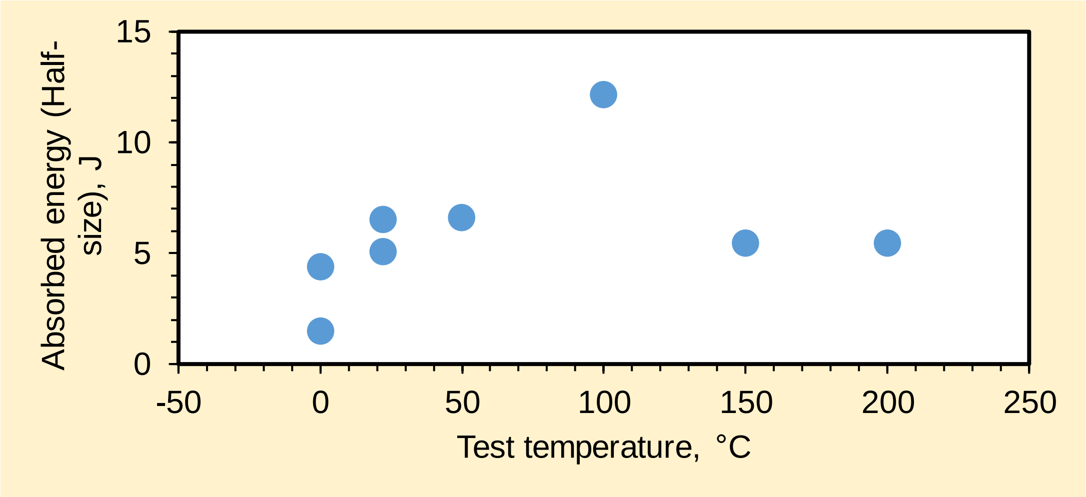

Figure 53: Charpy impact test results

An abnormality experienced in test six, at 100 °C, absorbed much higher energy than every other test specimen. The average calibrated absorption energy across all temperatures was 6.2625 J. The calibration is calculated based on the area percentage of the impacted bar, as shown in the 5th column of Table 10. The calculation is as follows, where W1 = Width including a notch, W2 = Width not including notch:

$$\text{Bar Formula} = \frac{\text{Dial energy (J)}}{\text{Area Percentage}} \qquad \text{Area Percentage} = \frac{((W1-0.039)*W4)}{((0.197-0.039)*0.197)} * 100$$

Figure 54: Charpy impact sample 1, 22ºC

Figure 55: Charpy impact sample 3, 0ºC

Figure 56: Charpy impact sample 6, 100ºC

Figure 57: Charpy impact sample 8, 200ºC

When comparing the impact toughness of WAAM RAFM samples to welded CLF-1 steels, the average impact toughness was closest to the two lowest impact energy tests recorded, at 3.3J and 4.3J, respectively. These both had a high heat input and, therefore, large delta ferrite formation, above 2.5% (Wu et al. 2020). The welding process examined in that study was electron beam and has a much higher power density than arc welding. The similar impact energy absorption indicated a strong presence of delta ferrite in the RAFM deposition samples. When comparing the failure characteristics of Figure 55 at 0ºC vs. Figure 56 at 100ºC, the ductility of the failure may be increasing. While the data does not continue to confirm this observation, as the absorption energy has only increased on the 100ºC test, the failure cross-section shows the presence of a limited amount of necking around the edges of the specimen.

CHAPTER 5: CONCLUSIONS

5.1 Conclusions of present work:

The capability to use WAAM to manufacture RAFM parts is reasonably developed. While the experimental samples would likely be unable to serve as a service part correctly, the real possibility of producing a part in this capacity has been established. The process development’s introduction of interpass temperature monitoring was unexpected; however, the testing showing that even cooling to below 300 °C caused no significant difference in the grain reformation was very beneficial to the eventual success of larger-scale deposition tests. The metallographic testing showed the majority of martensitic morphology and the presence of delta ferrite. When comparing the composition of the deposited material to that of cast samples, the morphology looks as expected, which helps to confirm the fusion of the powdered components in the wire to create the RAFM chemistry. The hardness data, averaging all interpass samples, is 423.74HV for the deposited material; this confirms the high presence of martensite formation occurring and provides insight into the lack of reformation in grains during the constant heat cycling of the material deposition layer by layer. We anticipated some form of tempering might occur by nature of the process, but it was unclear to what degree it would have an effect; at the current time, we can consider this effect negligible. The average resistance of 6.25J from the impact testing indicates a very brittle failure, which, compared to previous studies, was anticipated, and correlated to a more significant delta ferrite volume percent.

5.2 Recommendations for future work:

Further work on shielding gas selection would benefit the WAAM process with RAFM wire. The presence of porosities and inclusions in the welds was too high to be considered satisfactory; this lack of porosity control diminishes the possibility of feasibly producing parts for use at the current time. While different gasses were tested in the study, and 100% argon was found to have the potential to solve this issue, the print tests with 100% Argon were unsuccessful due to excessive heat buildup of the deposited material leading to geometric instability. Different process parameters or other shielding gas mixes with Argon may further the process towards total viability by eliminating the observed porosities. Further mechanical testing, such as the planned tensile tests, would be incredibly beneficial to determine the strengths of the deposited material fully, and radiation resistance testing would be of great interest to see how the process affects the material's ability to resist its effects compared to cast/machined parts.

An analysis of possible heat treatment procedures to further affect the microstructure may also be necessary. While no significant difference in the deposited layers was found, uniformity of the microstructure cannot be guaranteed in an as-deposited sample. Other studies conducted used heat treatments to increase the ductility of the welded RAFM steels; additionally, lowering the hardness would also aid in machinability for finishing the part.

REFERENCES

Abe, Takeyuki, and Hiroyuki Sasahara. 2016. “Dissimilar Metal Deposition with a Stainless Steel and Nickel-Based Alloy Using Wire and Arc-Based Additive Manufacturing.” *Precision Engineering* 45 (July): 387–95. https://doi.org/10.1016/j.precisioneng.2016.03.016.

Akers, Ryan, Preston Anderson, and Mike Barrett. n.d. “Waveform Comparison Between STT, CV and Power Mode GMAW Processes.” Accessed August 21, 2021. https://awo.aws.org/wp-content/uploads/posters2015/B/CategoryB-RyanAkers-HONORABLEMENTION.pdf.

Albert, S. K., K. Laha, A. K. Bhaduri, T. Jayakumar, and E. Rajendrakumar. 2016. “Development of IN-RAFM Steel and Fabrication Technologies for Indian TBM.” *Fusion Engineering and Design* 109–111: 1422–31. https://doi.org/10.1016/j.fusengdes.2015.12.005.

ASTM. n.d. “Standard Practice for Microetching Metals and Alloys.” https://doi.org/10.1520/E0407-07R15E01.

———. n.d. “Standard Test Methods and Definitions for Mechanical Testing of Steel Products.”

Aubert, P., F. Tavassoli, M. Rieth, E. Diegele, and Y. Poitevin. 2011a. “Low Activation Steels Welding with PWHT and Coating for ITER Test Blanket Modules and DEMO.” *Journal of Nuclear Materials* 409 (2): 156–62. https://doi.org/10.1016/j.jnucmat.2010.09.009.

———. 2011b. “Review of Candidate Welding Processes of RAFM Steels for ITER Test Blanket Modules and DEMO.” In *Journal of Nuclear Materials*, 417:43–50. https://doi.org/10.1016/j.jnucmat.2010.12.248.

Basuki, Widodo Widjaja, and Jarir Aktaa. 2011. “Investigation on the Diffusion Bonding of Tungsten and EUROFER97.” In *Journal of Nuclear Materials*, 417:524–27. https://doi.org/10.1016/j.jnucmat.2010.12.121.

Bellini, J, S Vezzu, and V Scappin. 2018. “Productive Technologies of Flux-Cored Wires by Welding.” WireTech World. 2018.

Chauhan, A., F. Bergner, A. Etienne, J. Aktaa, Y. de Carlan, C. Heintze, D. Litvinov, et al. 2017. “Microstructure Characterization and Strengthening Mechanisms of Oxide Dispersion Strengthened (ODS) Fe-9%Cr and Fe-14%Cr Extruded Bars.” *Journal of Nuclear Materials* 495 (November): 6–19. https://doi.org/10.1016/j.jnucmat.2017.07.060.

Chen, Jianguo, Chenxi Liu, Yongchang Liu, Biyu Yan, and Huijun Li. 2016. “Effects of Tantalum Content on the Microstructure and Mechanical Properties of Low-Carbon RAFM Steel.” *Journal of Nuclear Materials* 479 (October): 295–301. https://doi.org/10.1016/j.jnucmat.2016.07.029.

Chen, Xizhang, Yuming Huang, Bruce Madigan, and Jianzhong Zhou. 2012. "An Overview of the Welding Technologies of CLAM Steels for Fusion Application." *Fusion Engineering and Design* 87 (9): 1639–46. https://doi.org/10.1016/j.fusengdes.2012.06.009.

Chopra, O K, and A S Rao. n.d. "A REVIEW OF IRRADIATION EFFECTS ON LWR CORE INTERNAL MATERIALS-NEUTRON EMBRITTLEMENT, VOID SWELLING, AND IRRADIATION CREEP."

Das, Subhash, Jaykumar Vora, Vivek Patel, and Surender Bogum. 2021. "Experience with Advanced Welding Techniques (RMD & P-GMAW) with Seamless Metal Cored Wire for Oil & Gas Pipeline Industries." In *Journal of Physics: Conference Series*. Vol. 1950. IOP Publishing Ltd. https://doi.org/10.1088/1742-6596/1950/1/012043.

Dhinakaran, V., J. Ajith, A. Fathima Yasin Fahmidha, T. Jagadeesha, T. Sathish, and B. Stalin. 2020. "Wire Arc Additive Manufacturing (WAAM) Process of Nickel Based Superalloys-A Review." In *Materials Today: Proceedings*, 21:920–25. Elsevier Ltd. https://doi.org/10.1016/j.matpr.2019.08.159.

Ding, Donghong, Zengxi Pan, Dominic Cuiuri, and Huijun Li. 2015. "A Multi-Bead Overlapping Model for Robotic Wire and Arc Additive Manufacturing (WAAM)." *Robotics and Computer-Integrated Manufacturing* 31: 101–10. https://doi.org/10.1016/j.rcim.2014.08.008.

Eftink, Benjamin P., Daniel A. Vega, Osman el Atwani, David J. Sprouster, Yung Suk J. Yoo, Todd E. Steckley, Eda Aydogan, et al. 2021. "Tensile Properties and Microstructure of Additively Manufactured Grade 91 Steel for Nuclear Applications." *Journal of Nuclear Materials* 544 (February). https://doi.org/10.1016/j.jnucmat.2020.152723.

El-Atwani, O., B. P. Eftink, C. M. Cady, D. R. Coughlin, M. M. Schneider, and S. A. Maloy. 2021. "Enhanced Mechanical Properties of Additive Manufactured Grade 91 Steel." *Scripta Materialia* 199 (July). https://doi.org/10.1016/j.scriptamat.2021.113888.

Fava, Alessandra, Roberto Montanari, Maria Richetta, Claudio Testani, and Alessandra Varone. 2018. "Analysis of Strengthening Mechanisms in Nano-ODS Steel Depending on Preparation Route." *Journal of Material Science & Engineering* 07 (04). https://doi.org/10.4172/2169-0022.1000474.

Fu, J., J. C. Brouwer, R. W.A. Hendrikx, I. M. Richardson, and M. J.M. Hermans. 2020. "Microstructure Characterisation and Mechanical Properties of ODS Eurofer Steel Subject to Designed Heat Treatments." *Materials Science and Engineering A* 770 (January). https://doi.org/10.1016/j.msea.2019.138568.

Gaganidze, Ermile, Ferenc Gillemot, Ildiko Szenthe, Michael Gorley, Michael Rieth, and Eberhard Diegele. 2018. "Development of EUROFER97 Database and Material Property Handbook." *Fusion Engineering and Design* 135 (October): 9–14. https://doi.org/10.1016/j.fusengdes.2018.06.027.

Gelles, D, R Klueh, M Okada, and N Packan. 1990. “Reduced Activation Materials for Fusion Reactors.” *ASTM International STP 1047* 113.

Gelles, D. S., and M. L. Hamilton. 1987. “Effects of Irradiation on Low Activation Ferritic Alloys.” *Journal of Nuclear Materials* 148 (3): 272–78. https://doi.org/10.1016/0022-3115(87)90020-1.

Gheonea, M. C., D. Mihăilescu, S. N. Florescu, and E. Scutelnicu. 2018. “Experimental Research on Melting and Deposition Characteristics of Wires during Gas Metal Arc Welding.” In *IOP Conference Series: Materials Science and Engineering*. Vol. 400. Institute of Physics Publishing. https://doi.org/10.1088/1757-899X/400/2/022027.

Jiang, M. G., Z. W. Chen, J. D. Tong, C. Y. Liu, G. Xu, H. B. Liao, P. Wang, X. Y. Wang, M. Xu, and C. S. Lao. 2019. “Strong and Ductile Reduced Activation Ferritic/Martensitic Steel Additively Manufactured by Selective Laser Melting.” *Materials Research Letters* 7 (10): 426–32. https://doi.org/10.1080/21663831.2019.1631224.

Jun, Sun-Young, So-Young Im, Joonoh Moon, Chang-Hoon Lee, and Hyun-Uk Hong. 2020. “Technical Issues in Fusion Welding of Reduced Activation Ferritic/Martensitic Steels for Nuclear Fusion Reactors.” *Journal of Welding and Joining* 38 (1): 47–55. https://doi.org/10.5781/jwj.2020.38.1.5.

Kah, P., R. Suoranta, and J. Martikainen. 2013. “Advanced Gas Metal Arc Welding Processes.” *International Journal of Advanced Manufacturing Technology* 67 (1–4): 655–74. https://doi.org/10.1007/s00170-012-4513-5.

Klueh, R. L., and E. E. Bloom. 1985. “The Development of Ferritic Steels for Fast Induced-Radioactivity Decay for Fusion Reactor Applications.” *Nuclear Engineering and Design. Fusion* 2 (3): 383–89. https://doi.org/10.1016/0167-899X(85)90026-6.

Klueh, R. L., and A. T. Nelson. 2007. “Ferritic/Martensitic Steels for next-Generation Reactors.” *Journal of Nuclear Materials* 371 (1–3): 37–52. https://doi.org/10.1016/j.jnucmat.2007.05.005.

Laha, K., S. Saroja, A. Moitra, R. Sandhya, M. D. Mathew, T. Jayakumar, and E. Rajendra Kumar. 2013. “Development of India-Specific RAFM Steel through Optimization of Tungsten and Tantalum Contents for Better Combination of Impact, Tensile, Low Cycle Fatigue and Creep Properties.” *Journal of Nuclear Materials* 439 (1–3): 41–50. https://doi.org/10.1016/j.jnucmat.2013.03.073.

Lin, Zidong, Constantinos Goulas, Wei Ya, and Marcel J.M. Hermans. 2019. “Microstructure and Mechanical Properties of Medium Carbon Steel Deposits Obtained via Wire and Arc Additive Manufacturing Using Metal-Cored Wire.” *Metals* 9 (6). https://doi.org/10.3390/met9060673.

Liu, C. Y., J. D. Tong, M. G. Jiang, Z. W. Chen, G. Xu, H. B. Liao, P. Wang, X. Y. Wang, M. Xu, and C. S. Lao. 2019. “Effect of Scanning Strategy on Microstructure and Mechanical Properties of Selective Laser Melted Reduced Activation Ferritic/Martensitic Steel.”

Materials Science and Engineering A 766 (October). https://doi.org/10.1016/j.msea.2019.138364.

Liu, Sumei, Jinxing Sun, Haibao Zhou, Fei Wei, Mingxuan Lu, and Mingzhun Lei. 2019. “Experimental and Numerical Study on Fatigue Performance for TIG Welding and EB Welding of RAFM Steel Plate.” *Fusion Engineering and Design* 146 (September): 2663–66. https://doi.org/10.1016/j.fusengdes.2019.04.076.

Moravec, Jaromir, Tomasz Kik, and Iva Novakova. 2016. “Application of Numerical Simulations on X10CrWMoVNb9-2 Steel Multilayer Welding.” *MM Science Journal* 2016 (NOVEMBER): 1190–93. https://doi.org/10.17973/MMSJ.2016_11_201628.

Mori, H., H. Tanimura, R. Kiyoku, M. Fujiwara, T. Kato, T. Hirose, and H. Tanigawa. 2018. “Hot Crack Susceptibility in Multi-Pass Welds of Reduced Activation Ferritic/Martensitic Steel F82H.” *Journal of Nuclear Materials* 511 (December): 556–59. https://doi.org/10.1016/j.jnucmat.2018.06.016.

Mukherjee, Manidipto, Anupama Dutta, Prasanta Kanjilal, Tapan Kumar Pal, and Sunil Sisodia. 2015. “Enhancement of Microstructural and Mechanical Properties by Pulse Mode of Metal Transfer in Welded Modified Ferritic Stainless Steel.” *ISIJ International* 55 (7): 1439–47. https://doi.org/10.2355/isijinternational.55.1439.

Peng, Lei, Hongen Ge, Yong Dai, Qunying Huang, and Minyou Ye. 2016. “Microstructure and Microhardness of CLAM Steel Irradiated up to 20.8 Dpa in STIP-V.” *Journal of Nuclear Materials* 468 (January): 255–59. https://doi.org/10.1016/j.jnucmat.2015.11.023.

Praveen, P., P. K.D.V. Yarlagadda, and M. J. Kang. 2005. “Advancements in Pulse Gas Metal Arc Welding.” *Journal of Materials Processing Technology* 164–165 (May): 1113–19. https://doi.org/10.1016/j.jmatprotec.2005.02.100.

Raj, Baldev, and T. Jayakumar. 2011. “Development of Reduced Activation Ferritic-Martensitic Steels and Fabrication Technologies for Indian Test Blanket Module.” In *Journal of Nuclear Materials*, 417:72–76. https://doi.org/10.1016/j.jnucmat.2011.02.032.

Rodrigues, Tiago A., V. Duarte, R. M. Miranda, Telmo G. Santos, and J. P. Oliveira. 2019. “Current Status and Perspectives on Wire and Arc Additive Manufacturing (WAAM).” *Materials* 12 (7). https://doi.org/10.3390/ma12071121.

Rodrigues, Tiago A., V. R. Duarte, D. Tomás, Julian A. Avila, J. D. Escobar, Emma Rossinyol, N. Schell, Telmo G. Santos, and J. P. Oliveira. 2020. “In-Situ Strengthening of a High Strength Low Alloy Steel during Wire and Arc Additive Manufacturing (WAAM).” *Additive Manufacturing* 34 (August). https://doi.org/10.1016/j.addma.2020.101200.

Sam, Shiju, C. R. Das, V. Ramasubbu, S. K. Albert, A. K. Bhaduri, T. Jayakumar, and E. Rajendra Kumar. 2014. “Delta Ferrite in the Weld Metal of Reduced Activation Ferritic Martensitic Steel.” *Journal of Nuclear Materials* 455 (1–3): 343–48. https://doi.org/10.1016/j.jnucmat.2014.07.008.

Schaaf, B. van der, F. Tavassoli, C. Fazio, E. Rigal, E. Diegele, R. Lindau, and G. LeMarois. 2003. “The Development of EUROFER Reduced Activation Steel.” *Fusion Engineering and Design* 69 (1-4 SPEC): 197–203. https://doi.org/10.1016/S0920-3796(03)00337-5.

Seidel, K., R. A. Forrest, H. Freiesleben, V. D. Kovalchuk, D. v. Markovskij, D. v. Maximov, and S. Unholzer. 2002. “Experimental Investigation of Radioactivity Induced in the Fusion Power Plant Structural Material in Eurofer and in Other Steels by D–T Neutrons.” *Journal of Nuclear Materials* 307–311 (2 SUPPL.): 1037–41. https://doi.org/10.1016/S0022-3115(02)01292-8.

Shen, Jingjie, Yanfen Li, Feng Li, Huilong Yang, Zishou Zhao, Sho Kano, Yoshitaka Matsukawa, Yuhki Satoh, and Hiroaki Abe. 2016. “Microstructural Characterization and Strengthening Mechanisms of a 12Cr-ODS Steel.” *Materials Science and Engineering A* 673 (September): 624–32. https://doi.org/10.1016/j.msea.2016.07.030.

Silva, Leandro João da, Danielle Monteiro Souza, Douglas Bezerra de Araújo, Ruham Pablo Reis, and Américo Scotti. 2020. “Concept and Validation of an Active Cooling Technique to Mitigate Heat Accumulation in WAAM.” *International Journal of Advanced Manufacturing Technology* 107 (5–6): 2513–23. https://doi.org/10.1007/s00170-020-05201-4.

Silwal, B. n.d. “Effect of PWHT on the Toughness of HAZ for Grade 91 Steel.”

Silwal, B, L Li, A Deceuster, and B Griffiths. n.d. “Effect of PWHT on the Toughness of HAZ for Grade 91 Steel.”

Silwal, Bishal, Andrzej Nycz, and Mark Noakes. 2018. “The Effect of Shielding Gases on the Geometrical Features in Metal Big Area Additive Manufacturing (MBAAM).” www.osti.gov.

Ström, Petter, and Daniel Primetzhofer. 2021. “In-Situ Measurement of Diffusion and Surface Segregation of W and Ta in Bare and W-Coated EUROFER97 during Thermal Annealing.” *Nuclear Materials and Energy* 27 (June). https://doi.org/10.1016/j.nme.2021.100979.

Tan, L., Y. Yang, and J. T. Busby. 2013. “Effects of Alloying Elements and Thermomechanical Treatment on 9Cr Reduced Activation Ferritic-Martensitic (RAFM) Steels.” *Journal of Nuclear Materials* 442 (1-3 SUPPL.1). https://doi.org/10.1016/j.jnucmat.2012.10.015.

Tavassoli, A. A.F., E. Diegele, R. Lindau, N. Luzginova, and H. Tanigawa. 2014. “Current Status and Recent Research Achievements in Ferritic/Martensitic Steels.” *Journal of Nuclear Materials* 455 (1–3): 269–76. https://doi.org/10.1016/j.jnucmat.2014.06.017.

Tavassolit, A A. n.d. “Characterization of 316L Steel Welded Joints Irradiated Between 15 to 41 Dpa.”

Ugla, Adnan. n.d. “Metal-Inert-Gas-Welding-Based-Shaped-Metal-Deposition-in-Additive-Layered-Manufacturing-a-Review.”

Vallant, Rudolf. n.d. "Welding of Ultra High-Strength Steel (UHSS) With Austenitic Metal Powder Wire (MPW)." https://www.researchgate.net/publication/266870755.

Vasantharaja, P., M. Vasudevan, and P. Parameswaran. 2019. "Effect of Welding Techniques on the Microstructure and Mechanical Properties of Reduced Activation Ferritic-Martensitic (RAFM) Steel Weld Joints." *Fusion Engineering and Design* 148 (November). https://doi.org/10.1016/j.fusengdes.2019.111289.

Wang, G., P. G. Huang, and Y. M. Zhang. 2004. "Numerical Analysis of Metal Transfer in Gas Metal Arc Welding under Modified Pulsed Current Conditions." *Metallurgical and Materials Transactions B: Process Metallurgy and Materials Processing Science* 35 (5): 857–66. https://doi.org/10.1007/s11663-004-0080-y.

Wang, Jian, Jinpeng Zhou, Xiaofeng Lu, and Lei Cui. 2020. "Restraining Method for Delta Ferrite in 9Cr-RAFM Welded Joint." *Fusion Engineering and Design* 158 (September). https://doi.org/10.1016/j.fusengdes.2020.111722.

Wang, Wei, Gang Xu, and Liangliang Song. 2019. "Long-Term Stability of Precipitated Phases in CLAM Steel during Thermal Aging." *Journal of Nuclear Materials* 521 (August): 56–62. https://doi.org/10.1016/j.jnucmat.2019.04.034.

Williams, S. W., F. Martina, A. C. Addison, J. Ding, G. Pardal, and P. Colegrove. 2016. "Wire + Arc Additive Manufacturing." *Materials Science and Technology (United Kingdom)* 32 (7): 641–47. https://doi.org/10.1179/1743284715Y.0000000073.

Wu, Bintao, Zengxi Pan, Donghong Ding, Dominic Cuiuri, Huijun Li, Jing Xu, and John Norrish. 2018. "A Review of the Wire Arc Additive Manufacturing of Metals: Properties, Defects and Quality Improvement." *Journal of Manufacturing Processes*. Elsevier Ltd. https://doi.org/10.1016/j.jmapro.2018.08.001.

Wu, Qianru, Zhenshu Ma, Guangsen Chen, Changmeng Liu, Dongxi Ma, and Shuyuan Ma. 2017. "Obtaining Fine Microstructure and Unsupported Overhangs by Low Heat Input Pulse Arc Additive Manufacturing." *Journal of Manufacturing Processes* 27 (June): 198–206. https://doi.org/10.1016/j.jmapro.2017.05.004.

Wu, Shikai, Yilei Shi, Guoyu Zhang, Song Zhang, Hongbin Liao, Xiaoyu Wang, and Zhiyun Qin. 2020a. "Improving Impact Toughness of Heavy Section Reduced Activation Ferritic Martensitic CLF-1 Steel Joints with Electron Beam Welding." *Journal of Nuclear Materials* 531 (April): 152031. https://doi.org/10.1016/J.JNUCMAT.2020.152031.

———. 2020b. "Improving Impact Toughness of Heavy Section Reduced Activation Ferritic Martensitic CLF-1 Steel Joints with Electron Beam Welding." *Journal of Nuclear Materials* 531 (April): 152031. https://doi.org/10.1016/J.JNUCMAT.2020.152031.

Xia, Chunyang, Zengxi Pan, Joseph Polden, Huijun Li, Yanling Xu, Shanben Chen, and Yuming Zhang. 2020. "A Review on Wire Arc Additive Manufacturing: Monitoring, Control and a Framework of Automated System." *Journal of Manufacturing Systems*. Elsevier B.V. https://doi.org/10.1016/j.jmsy.2020.08.008.

Xue, Bing, Weining Lei, Xiao Liu, and Shixin Chen. 2020. “Effect of Medium Entropy Alloy Powder-Core Wire on Friction Wear and Corrosion Resistance of Arc Cladding Additive Layer.” *Materials Research Express* 7 (7). https://doi.org/10.1088/2053-1591/aba84f.

Zheng, Pengfei, Yanfen Li, Jiarong Zhang, Jingjie Shen, Takuya Nagasaka, Takeo Muroga, and Hiroaki Abe. 2020. “On the Thermal Stability of a 9Cr-ODS Steel Aged at 700 °C up to 10000 h - Mechanical Properties and Microstructure.” *Materials Science and Engineering A* 783 (May). https://doi.org/10.1016/j.msea.2020.139292.

APPENDIX

KUKA KRL CODE TO PRINT MULTILAYER WALL, VARIABLE DECLARATION AND POINT TRACE SECTION

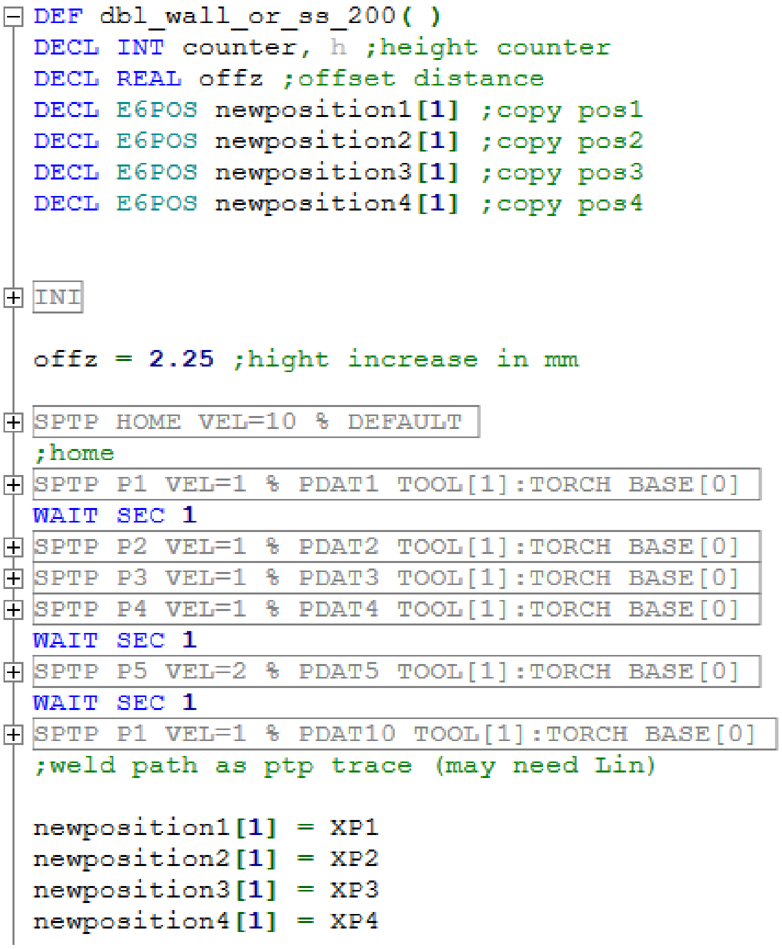

```
DEF dbl_wall_or_ss_200( )
DECL INT counter, h ;height counter
DECL REAL offz ;offset distance
DECL E6POS newposition1[1] ;copy pos1
DECL E6POS newposition2[1] ;copy pos2
DECL E6POS newposition3[1] ;copy pos3
DECL E6POS newposition4[1] ;copy pos4


INI

offz = 2.25 ;hight increase in mm

SPTP HOME VEL=10 % DEFAULT
;home
SPTP P1 VEL=1 % PDAT1 TOOL[1]:TORCH BASE[0]
WAIT SEC 1
SPTP P2 VEL=1 % PDAT2 TOOL[1]:TORCH BASE[0]
SPTP P3 VEL=1 % PDAT3 TOOL[1]:TORCH BASE[0]
SPTP P4 VEL=1 % PDAT4 TOOL[1]:TORCH BASE[0]
WAIT SEC 1
SPTP P5 VEL=2 % PDAT5 TOOL[1]:TORCH BASE[0]
WAIT SEC 1
SPTP P1 VEL=1 % PDAT10 TOOL[1]:TORCH BASE[0]
;weld path as ptp trace (may need Lin)

newposition1[1] = XP1
newposition2[1] = XP2
newposition3[1] = XP3
newposition4[1] = XP4
```

KUKA KRL CODE TO PRINT MULTILAYER WALL, FOR LOOP SECTION

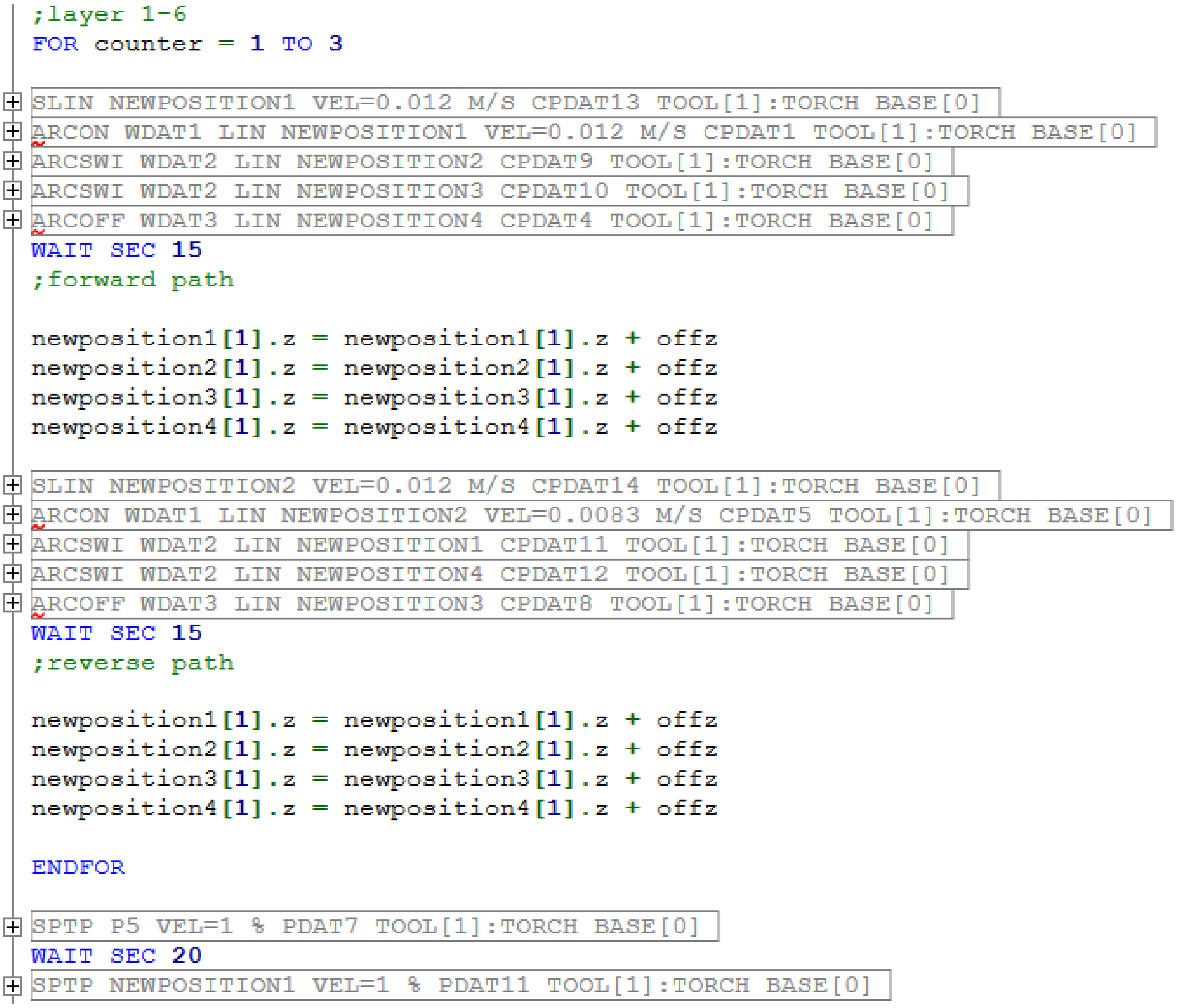

```
;layer 1-6
FOR counter = 1 TO 3

SLIN NEWPOSITION1 VEL=0.012 M/S CPDAT13 TOOL[1]:TORCH BASE[0]
ARCON WDAT1 LIN NEWPOSITION1 VEL=0.012 M/S CPDAT1 TOOL[1]:TORCH BASE[0]
ARCSWI WDAT2 LIN NEWPOSITION2 CPDAT9 TOOL[1]:TORCH BASE[0]
ARCSWI WDAT2 LIN NEWPOSITION3 CPDAT10 TOOL[1]:TORCH BASE[0]
ARCOFF WDAT3 LIN NEWPOSITION4 CPDAT4 TOOL[1]:TORCH BASE[0]
WAIT SEC 15
;forward path

newposition1[1].z = newposition1[1].z + offz
newposition2[1].z = newposition2[1].z + offz
newposition3[1].z = newposition3[1].z + offz
newposition4[1].z = newposition4[1].z + offz

SLIN NEWPOSITION2 VEL=0.012 M/S CPDAT14 TOOL[1]:TORCH BASE[0]
ARCON WDAT1 LIN NEWPOSITION2 VEL=0.0083 M/S CPDAT5 TOOL[1]:TORCH BASE[0]
ARCSWI WDAT2 LIN NEWPOSITION1 CPDAT11 TOOL[1]:TORCH BASE[0]
ARCSWI WDAT2 LIN NEWPOSITION4 CPDAT12 TOOL[1]:TORCH BASE[0]
ARCOFF WDAT3 LIN NEWPOSITION3 CPDAT8 TOOL[1]:TORCH BASE[0]
WAIT SEC 15
;reverse path

newposition1[1].z = newposition1[1].z + offz
newposition2[1].z = newposition2[1].z + offz
newposition3[1].z = newposition3[1].z + offz
newposition4[1].z = newposition4[1].z + offz

ENDFOR

SPTP P5 VEL=1 % PDAT7 TOOL[1]:TORCH BASE[0]
WAIT SEC 20
SPTP NEWPOSITION1 VEL=1 % PDAT11 TOOL[1]:TORCH BASE[0]
```

MICROHARDNESS TEST RESULTS FOR INTERPASS TEMPERATURE TESTS

Base Sample		20S Sample		40S Sample		300ºC Sample	
Hardness (HV)	Distance (mm)	Hardness (HV)	Distance (mm)	Hardness (HV)	Distance (mm)	Hardness (HV)	Distance (mm)
208.6	0	197.7	0	289.4	0	185.4	0
404.4	0.15	415.5	0.12	430.7	0.13	396.5	0.13
405.9	0.3	415.5	0.25	441.3	0.27	415.5	0.26
446.7	0.42	408.2	0.37	413.1	0.45	413.1	0.38
438.6	0.54	392	0.5	455	0.58	418	0.5
444	0.74	430.7	0.62	420.5	0.71	398.8	0.63
449.4	0.86	418	0.74	401.2	0.89	435.9	0.76
418	0.96	423	0.86	444	1.02	423	0.88
428.1	1.1	433.3	0.98	401.2	1.14	436.7	1.01
428.1	1.27	385.3	1.1	428.1	1.35	423	1.13
438.6	1.35	420.5	1.22	418	1.48	408.2	1.26
418	1.43	418	1.34	428.1	1.65	403.5	1.38
443.3	1.55	425.5	1.47	405.9	1.87	420.5	1.5
441	1.73	425.5	1.6	394.3	2	420.5	1.63
433.3	1.81	449.4	1.71	425.5	2.12	438.6	1.76
418	1.92	405.9	1.84	433.3	2.25	449.4	1.88
428.1	2.06	418	1.97	433.3	2.38	441.3	2
425.1	2.28	438.6	2.09	478.4	2.62	475.4	2.13
		428.1	2.23	405.9	2.79	435.4	2.26
		425.5	2.45			420.5	2.39
		433.3	2.52			423	2.5
		403.7	2.63			392.2	2.63
		410.7	2.75			441.3	2.76
		396.5	2.9			405.9	2.88

CHARPY IMPACT SAMPLE MATERIAL HRC HARDNESS TEST DATA

Charpy Sample Height (in)	Side 1 hardness (HRC)	Side 2 hardness (HRC)
0	13.5	13.5
0.125	42.25	43.5
0.25	40.5	35.5
0.375	35	35
0.5	42.5	43
0.625	37.5	32.5
0.75	32.5	43.75
0.875	39	30.5
1	41.5	42.5
1.125	39.75	41

TENSILE SAMPLE, HRC HARDNESS TEST DATA

Tensile Sample Height (in)	Hardness (HRC)
0	42.5
0.125	37.5
0.25	23.5
0.375	44.5
0.5	33
0.625	37.75
0.75	38.5
0.875	44.25
1	32
1.125	43
1.25	44
1.375	43.5
1.5	36
1.625	40.5
1.75	44.5
1.875	34
2	36
2.125	41.5
2.25	44.5
2.375	34
2.5	33
2.625	43.5
2.75	37.75
2.875	32
3	33
3.125	40.5
3.25	45.5
3.375	35.5
3.5	38.5
3.625	42